

# Beyond Protocols: Understanding the Electrical Behavior of Perovskite Solar Cells by Impedance Spectroscopy

Elnaz Ghahremanirad, Osbel Almora,\* Sunil Suresh, Amandine A. Drew, Towhid H. Chowdhury, and Alexander R. Uhl\*

Impedance spectroscopy (IS) is an effective characterization technique used to probe and distinguish charge dynamics occurring at different timescales in optoelectronic and electric devices. With the rapid rise of research being conducted on perovskite solar cells (PSCs), IS has significantly contributed to the understanding of their device performance and degradation mechanisms, including metastable effects such as current–voltage hysteresis. The ionic–electronic behavior of PSCs and the presence of a wide variety of perovskite compositions and cell architectures add complexity to the accurate interpretation of the physical processes occurring in these devices. In this review, the most common IS protocols are explained to help perform accurate impedance measurements on PSC devices. It critically reviews the most commonly used equivalent circuits alongside drift-diffusion modeling as a complementary technique to analyze the impedance response of PSCs. As an emerging method for characterizing the interfacial recombination between the perovskite layer and selective contacts, light intensity modulated impedance spectroscopy technique is further discussed. Lastly, important works on the application of IS measurement protocols for PSCs are summarized followed by a detailed discussion, providing a critical perspective and outlook on the growing topic of IS on PSCs.

## 1. Introduction

Perovskite solar cells (PSCs) were first introduced to the photovoltaic research field over a decade ago with the inclusion of metal halide perovskites as the light absorber material.<sup>[1]</sup> Since then, PSCs have shown an unprecedented increase in power conversion efficiencies (PCEs), from 3.8% in 2009 to 26.08% in 2023.<sup>[2]</sup> Notably, the PCEs are now approaching the record efficiency of market leading single crystalline silicon solar cells at 26.8%.<sup>[3]</sup> The success of PSCs is attributed to the easy and low-cost fabrication methods and favorable optoelectronic properties of organic/inorganic hybrid lead (Pb) halide perovskites.<sup>[4–6]</sup> Moreover, the wide range of band gap tunability of thin-film perovskite materials make them suitable for multijunction and semi-transparent architectures.<sup>[4–6]</sup> However, despite the indisputable progress, intrinsic device stability is still an issue that limits the commercialization of PSCs.


In particular, the dual electronic–ionic conductivity of the hybrid lead halide perovskites remains a subject of intense research and debate.<sup>[7–9]</sup> The ionic and electronic processes within PSCs are closely interconnected and partly overlap at different measurement timescales. This makes it difficult to discern between various electronic processes in the PSC related to bulk phenomena, interface, and/or grain boundaries (GBs). In addition, slow contributions from ionic features of the halide perovskite crystals enhance the timescale of the electric response,<sup>[10]</sup> which is evidenced by the hysteresis phenomena of the current density–voltage ( $J$ – $V$ ) curve of PSCs.<sup>[11,12]</sup>

Distinguishing ionic–electronic phenomena in PSCs requires an appropriate tuning of the timescale for each process to resolve their overlap. In general, these approaches can either be made in the time or frequency domain. In the time domain, transient measurements include transient photovoltage (TPV),<sup>[13,14]</sup> transient photocurrent (TPC),<sup>[15]</sup> or deep level transient spectroscopy (DLTS).<sup>[16]</sup> These techniques are very effective in exploring recombination and trap related features by relying on exponential decay functions to determine characteristic response times ( $\tau$ ). Alternatively, typical measurements in the frequency domain in-

E. Ghahremanirad, S. Suresh, A. A. Drew, T. H. Chowdhury, A. R. Uhl  
Laboratory for Solar Energy and Fuels (LSEF)  
School of Engineering  
The University of British Columbia  
Kelowna V1V1V7, Canada  
E-mail: alexander.uhl@ubc.ca

O. Almora  
Department of Electrical  
Electronic and Automatic Engineering  
Universitat Rovira i Virgili, Tarragona 43007, Spain  
E-mail: osbel.almora@urv.cat

O. Almora  
Institute of Advanced Materials  
Universitat Jaume I, Castelló 12006, Spain

 The ORCID identification number(s) for the author(s) of this article can be found under <https://doi.org/10.1002/aenm.202204370>

© 2023 The Authors. Advanced Energy Materials published by Wiley-VCH GmbH. This is an open access article under the terms of the Creative Commons Attribution-NonCommercial-NoDerivs License, which permits use and distribution in any medium, provided the original work is properly cited, the use is non-commercial and no modifications or adaptations are made.

DOI: 10.1002/aenm.202204370

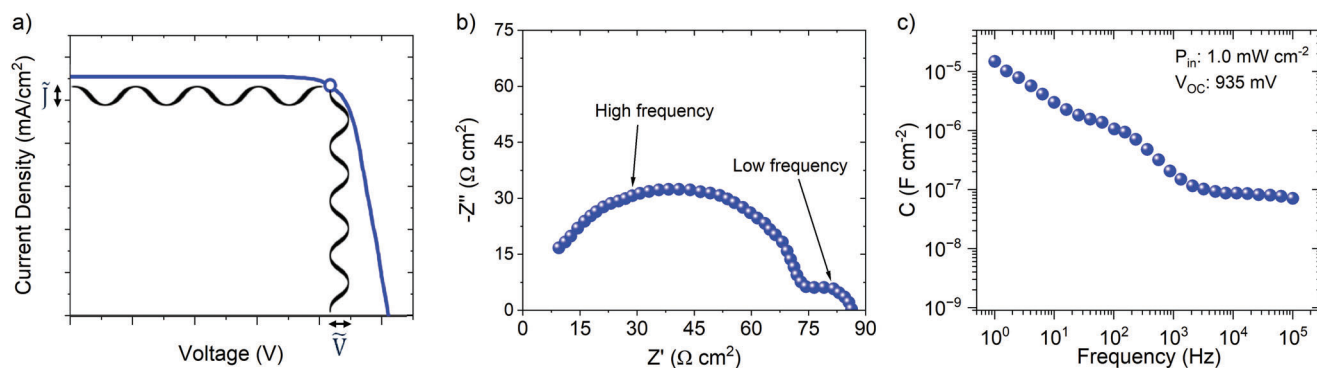


**Figure 1.** a) Schematic representation of the impedance spectroscopy (IS) measurement at maximum power point (MPP) for a solar cell under illumination with respect to the corresponding  $J$ - $V$  curve; b) Nyquist plot ( $-Z''$  vs  $Z'$ ) comprises of two well-separated timescales at high and low frequencies (HF and LF) measured at open-circuit (OC) under 0.01 sun illumination intensity; and c) capacitance-frequency plot shows two plateaus at low and high frequencies, LF and HF, respectively. Reproduced with permission.<sup>[23]</sup> Copyright 2020, Elsevier.

clude impedance spectroscopy (IS) and light intensity-modulated photocurrent/photovoltage spectroscopy (IMPS/IMVS), which are usually parameterized via equivalent circuit (EC) theory. Notably, the IS analysis can provide insights on recombination and trap-related features which also discern several phenomena at different timescales in the bulk and at the interfaces.

Potentiostatic IS analyses are conducted by measuring an alternating current mode (AC) current density signal ( $\tilde{j}$ ) upon an AC voltage perturbation ( $\tilde{V}$ ) (see **Figure 1a**) in a range of frequencies ( $f$ ) (e.g., from 1 kHz to 1 MHz). Provided the condition of linearity, potentiostatic IS analyses allow for the extraction of the impedance measurement  $Z = \tilde{V}/\tilde{j}$  whose real and imaginary parts provide information on the energy dissipation and storage features, typically as resistance ( $R$ ) and capacitance ( $C$ ), respectively. Comprehensive studies on the basics of IS in solar cells have been published.<sup>[17,18]</sup> **Figure 1b,c** illustrates a typical Nyquist and capacitance-frequency ( $C$ - $f$ ) Bode plot of a PSC, respectively. Most of the impedance spectra of PSCs comprise two or three arcs in the impedance Nyquist plot and two or three plateaus in the  $C$ - $f$  plot which represent the real part of the capacitance versus frequency in logarithmic scale.<sup>[18]</sup> More complicated spectra include features such as further resistance-capacitance  $R$ - $C$  arcs/plateaus, negative capacitances,<sup>[19,20]</sup> and/or inductive loops can be observed in the Nyquist plots.<sup>[21,22]</sup> Negative capacitance refers to the low frequency arc below the real  $Z'$ -axis ( $Z'$ ) and inductive loop appears as two arcs crossing each other at the intermediate/low frequencies (see Section 1.3). Depending on the frequency range of the spectra or measurement conditions (e.g., bias, illumination, temperature), several protocols have been implemented for IS characterizations.

Notably, the graphical representation of IS data, such as the use of linear and logarithmic 1:1 aspect ratio for the Nyquist and Bode plots, respectively, can support the analysis of IS measurements. For instance, when looking at the imaginary part as a function of the real part of impedance in the Nyquist plot, perfect circular shapes refer to  $R$ - $C$  constants in the EC models, while modifications can suggest the need to consider different EC elements. Similarly, each plateau in the Bode plot of capacitance

informs on an  $R$ - $C$  constant, and the transition shape between these plateaus may suggest the best fit for selecting EC elements for modeling. For instance, using a semi-log capacitance Bode plot with only the frequency axis on log scale may hinder the identification of intermediate-frequency features in the capacitance spectra.

**Table 1** summarizes the wide family of IS characterization routines and the corresponding measurement conditions, expected parameters, and related theories, used for the study of PSCs. It is worth noting that the variations in illumination intensity, temperature ( $T$ ), frequency, and direct-current (DC) mode voltage ( $\bar{V}$ ) explore different optoelectronic features, and wider the ranges for each parameter, higher the consistency of the IS study results. Commonly used characterization routines include IS measurements under dark condition at variable  $\bar{V}$ , capacitance spectroscopy (CS),<sup>[24,25]</sup> Mott-Schottky (M-S),<sup>[26,27]</sup> thermal admittance spectroscopy (TAS),<sup>[28]</sup> the herein termed open-circuit recombination analysis by impedance spectroscopy (ORIS),<sup>[23,29]</sup> and equivalent circuit-oriented impedance spectroscopy (ECIS).<sup>[30]</sup> Review articles have recently discussed the impact and importance of IS for PSCs, are summarized in **Table S1**, Supporting Information.

In this article, Section 1 describes the latest progress on the use of IS protocols (see **Table 1**) for PSC applications. Section 2 is dedicated to elucidating these protocols including IS measurements in dark at a DC bias, capacitance spectroscopy, M-S analysis, and TAS, (Section 2.1) followed by IS measurements under illumination at open-circuit (OC) condition (Section 2.2), and equivalent circuit modeling (Section 2.3). In Section 3, drift-diffusion (DD) modeling of IS spectra along with some recent progress is reviewed. Section 4 is devoted to describing the concept of light intensity modulated impedance spectroscopy (LIMIS). The application of IS in analyzing the role of bulk and interfaces of the perovskite layer on the performance of PSCs will be presented in Section 5. This section intends to provide progress on the use of the above protocols and analyses to elucidate prevalent phenomena in PSCs of different morphologies, structures, and materials. To conclude, Section 6 provides suggestions and recommendations from the authors to guide and inform future work in the area.

**Table 1.** Typical characterization protocols based on impedance spectroscopy (IS) for perovskite solar cells (PSCs).

Protocol	Section	Conditions	Expected parameters	Theory comments	Ref.
Dark measurement at different DC biases	2.1.1	Dark, room temperature, forward bias	Recombination resistance ( $R_{rec}$ ), transport resistance ( $R_{tr}$ )	EC	[22]
Capacitance spectroscopy (CS)	2.1.2	Dark, variable $T$ , high $f$ spectrum	Dielectric constant ( $\epsilon_r$ ), characteristic phase transition temperatures ( $T_{pt}$ ), sample thickness ( $L$ )	EC	[18,24,31]
Mott–Schottky (M–S) analysis	2.1.3	Dark, variable $\bar{V} < V_{bi}$ , fixed high $f$	Concentration of acceptor ( $N_A$ ) or donor ( $N_D$ ) shallow level doping defects ( $N$ ), built-in potential ( $V_{bi}$ ), depletion layer width ( $w_{dl}$ )	p–n junction samples. metal/semiconductor contacts	[26]
Thermal admittance spectroscopy (TAS)	2.1.4	Dark, variable $T$ , $f$ spectrum	Trap density ( $N_t$ ), trap energy ( $E_t$ ) and capture cross section ( $\sigma_t$ ) of deep level trap defects, density of states (DOS)	Only in p–n junction samples	[28]
Open-circuit recombination analysis by impedance spectroscopy (ORIS)	2.2	Quasi-open-circuit regime, variable light intensity, variable $\bar{V}$ , $f$ spectrum	Recombination resistance ( $R_{rec}$ ), recombination lifetime ( $\tau_{rec}$ ), chemical capacitance ( $C_{\mu}$ ), ideality factor ( $n_{id}$ )	EC, Shockley equation, only in solar cells	[23,29]
Equivalent circuit-oriented impedance spectroscopy (ECIS)	2.3	$f$ spectrum	Conductivity ( $\sigma$ ), Jonscher's power ( $n_e$ ), resistivity ( $\rho$ ), series resistance ( $R_s$ ), shunt resistance ( $R_{sh}$ ), geometric capacitance ( $C_g$ )	EC	[30]

## 2. Common IS Measurement Protocols for Perovskite Solar Cells

### 2.1. Measurements under Dark Conditions

IS measurements in dark condition comprise techniques which are performed under the exclusion of light irradiation at either a single bias or a range of bias voltages. This is particularly useful for PSCs, as photogeneration of charge carriers under illumination may enhance the mobile ion density or mobility of charge carriers,<sup>[5]</sup> thereby changing their kinetics and overall transport properties within the device. Importantly, dark IS data analysis can be used to infer correlations between device performance, and its resistive and/or capacitive features. Subsequently, for dark IS measurements, PSCs are typically placed inside a Faraday cage to preclude the device from ambient light and external electromagnetic fields. Consequently, higher stability for PSCs is observed in dark conditions, which also reduces PSC degradation during IS measurements.<sup>[32,33]</sup> Besides, to study charge carrier dynamics under dark, encapsulating the PSC or measuring under dry air or nitrogen may mitigate the effects of ambient conditions that degrade the device, resulting in device instability.<sup>[34,35]</sup>

#### 2.1.1. Dark Measurement at Different DC Biases

In this method, a DC bias is applied to a solar cell under dark condition, and the current response is measured in response to a small AC perturbation over a frequency range, commonly between 0.1 Hz–1 MHz. Typical IS spectra from dark IS measurements upon applying a DC bias show two main time constants (two semicircles in the Nyquist plot) in the low and high frequency region, respectively. Important parameters, such as series resistance ( $R_s$ ), recombination resistance ( $R_{rec}$ ) and transport

resistances ( $R_{tr}$ ) can be extracted from these measurements. Series resistance is typically extracted from the first  $Z'$ -axis intercept of the high frequency arc in Nyquist representation. It is commonly related to the resistance losses from device contacts, and measurement-related electrical resistances, including transparent conductive oxides (TCOs), electrodes, and connection wires.<sup>[36–38]</sup> The second  $Z'$ -axis intercept of the high frequency arc is correlated with the high frequency resistance ( $R_{Hf}$ ) and the high resistance intercept of the low-frequency arc is termed as low frequency resistance ( $R_{Lf}$ ).  $R_{Hf}$  is commonly correlated with fast electronic processes such as carrier generation, radiative recombination, trap-assisted recombination, and transport.<sup>[36,39]</sup> Notably, dominant contributions on  $R_{Hf}$  are dependent on illumination conditions.

In dark condition,  $R_{Hf}$  is commonly related to  $R_{tr}$  in the bulk of perovskite; while under illumination and high photoconductivity, both  $R_{Lf}$  and  $R_{Hf}$  can be attributed to  $R_{rec}$  on account of negligible contribution of  $R_{tr}$  to the impedance response in high performance PSCs.<sup>[40,41]</sup>  $R_{Lf}$  is mostly related to slow processes such as migration of positive or negative ions and/or vacancies which leads to ion and/or vacancy accumulation at the interfaces of perovskite with hole transport layer (HTL) and/or electron transport layer (ETL) impeding charge transport and transfer.<sup>[36,40]</sup> Therefore, due to mixed contributions of ionic and electronic phenomena in the low frequency region and the dependence of low frequency features on the architecture of PSCs and the measurement conditions, this part of the impedance spectra in PSCs is still debated.

In a study by Sangwan et al., dark IS measurements over a DC bias range from 0 to 1 V and frequencies from 1 Hz to 1 MHz were performed for planar PSCs with different hole transport materials (HTMs) to elucidate carrier kinetics at lower frequencies and to understand  $J$ – $V$  hysteresis and instability of PSCs.<sup>[22]</sup>

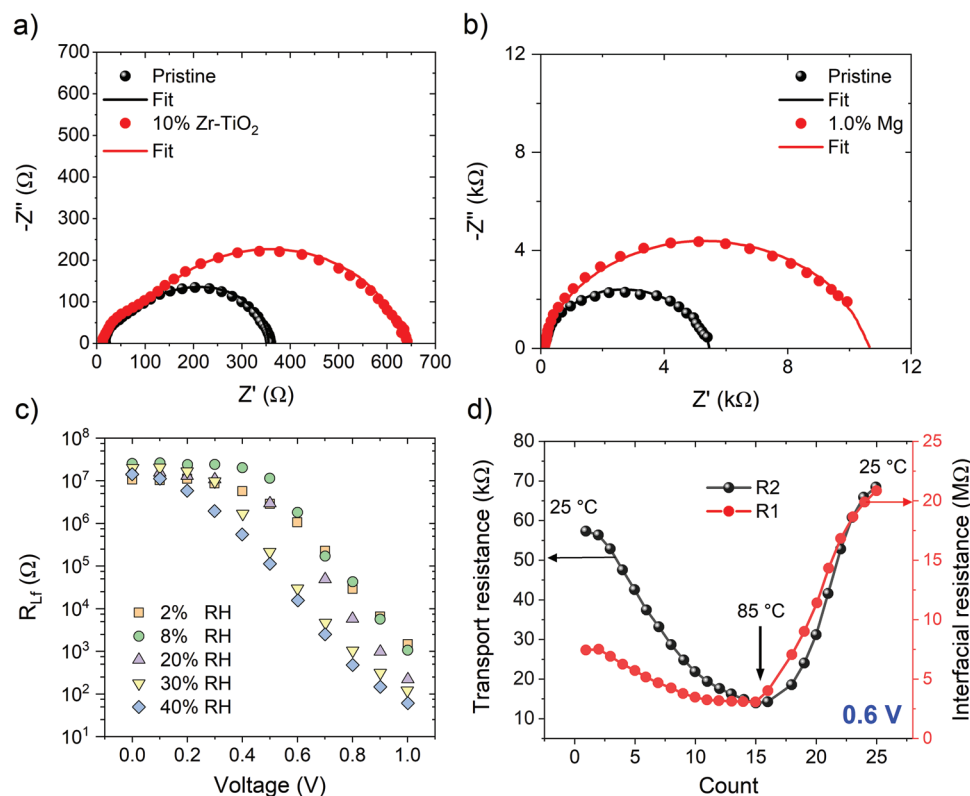


**Figure 2.** a) The Nyquist plots of pristine and Zr-doped  $\text{TiO}_2$  PSCs showing a lower recombination rate in the latter case based on the low frequency response measured in the dark at a bias of 1.0 V. Reproduced with permission.<sup>[44]</sup> Copyright 2021, Elsevier. b) The Nyquist plots of pristine and 1.0% Mg-doped PSC measured at the applied bias of 0.7 V under dark condition. Reproduced with permission.<sup>[46]</sup> Copyright 2018, American Chemical Society. c) The impact of relative humidity (RH) on the low frequency  $R_{\text{rec}}$  as a function of voltage for a planar FAPbI<sub>3</sub> (FA: formamidinium) PSC. Reproduced with permission.<sup>[47]</sup> Copyright 2015, American Chemical Society. d) IS measurement under dark condition at the applied bias of 0.6 V and 25–85 °C temperature cycle showing the variation of transport and interfacial resistances as a function of measurement cycle. Reproduced with permission.<sup>[39]</sup> Copyright 2020, American Chemical Society.

IS analysis at low frequencies showed lower  $R_{\text{rec}}$  (i.e., higher recombination rate) for the poly(triaryl amine) (PTAA)-based PSCs compared to 2,2',7,7'-tetrakis(*N,N*-di-*p*-methoxyphenylamine)9,9'-spirobifluorene (Spiro-OMeTAD)-based PSCs, which is in accordance with the lower performance of PTAA-based PSCs ( $\approx 10\%$  vs  $\approx 15\%$  PCE). The assessment of hysteresis with IS has been discussed in recent studies.<sup>[19,42,43]</sup> Gonzales et al., formulated a general model to correlate IS data and device hysteresis at different voltages of the  $J$ - $V$  curve in PSCs.<sup>[42]</sup> The model was used to evaluate hysteresis via the impedance parameters and track transitions between capacitive and inductive domains at low and high voltages, respectively.

Sandhu et al., employed dark IS analysis to study the influence of doping on electron transport layers for PSC applications.<sup>[44]</sup> The Nyquist plot in **Figure 2a** shows two distinct arcs with an enhanced low frequency resistance for the Zr-doped  $\text{TiO}_2$  based PSCs, which was related to the higher conductivity of the Zr- $\text{TiO}_2$  layer compared to a pristine  $\text{TiO}_2$  layer. Subsequently, due to improved charge carrier collection at the Zr- $\text{TiO}_2$ /perovskite interface, the  $J_{\text{SC}}$  improved from 22.04 to 23.57  $\text{mA cm}^{-2}$ . Besides doping the charge transport layers, doping or modification of perovskite materials can be useful to improve crystal quality, charge transport, charge collection, and trap passivation.<sup>[44]</sup> In this regard, Liao et al., investigated the role of graphitic car-

bon nitride ( $g\text{-C}_3\text{N}_4$ ) as an additive to methylammonium lead iodide (MAPbI<sub>3</sub>) based precursor ink and fabricated PSCs. The respective PSCs were characterized by means of dark IS from 0.8 to 1.0 V.<sup>[45]</sup>

The authors reported that the  $g\text{-C}_3\text{N}_4$  containing PSC showed increased  $R_{\text{rec}}$  values and longer carrier lifetime. The authors attributed this improvement to effective trap passivation and facilitated charge extraction and collection by  $g\text{-C}_3\text{N}_4$ . Likewise, Yang et al., performed IS analysis under dark condition at a bias of 0.7 V to show the influence of doping MAPbI<sub>3</sub> with 1% of Mg.<sup>[46]</sup> The impedance results shown in **Figure 2b** present a larger  $R_{\text{rec}}$  for the 1% Mg treated device which was attributed to the formation of large-grained, pinhole-free perovskite films.

Two important factors, such as relative humidity (RH) and temperature can affect the performance of PSCs during measurements. It was reported that the presence of  $\text{H}_2\text{O}$ , and possibly  $\text{O}_2$  can trigger a reaction with the perovskite compound.<sup>[48]</sup> The presence of humidity can alter the optical properties of the perovskite films by deteriorating the morphology of the films due to reduced film crystallinity.<sup>[47,49]</sup> Wozny et al., studied dark impedance analysis over the voltage range of 0–1 V and demonstrated decreased  $R_{\text{Lf}}$ , and  $R_{\text{rec}}$ , with increasing the RH levels (**Figure 2c**).<sup>[47]</sup> Interestingly, even though  $R_{\text{Lf}}$  was reduced, the predominant interface recombination mechanism was not significantly affected

considering PSC ideality factors ( $n_{id}$ ). Assuming  $R_{Lf} \approx R_{rec} \propto \exp[-qV_{oc}/n_{id}k_B T]$ ,<sup>[29]</sup> ideality factors were determined to  $n_{id} \approx 2.0$  and 1.7 at 2% and 40% RH, respectively. This may indicate the major importance of proton densities and their impact on the electric response.<sup>[48]</sup>

The influence of temperature on the performance of PSCs by comparing dark IS on PSCs at 0.6 V at temperatures ranging from 25 to 85 °C has been investigated by Feng et al.,<sup>[39]</sup> Figure 2d depicts the change of both low frequency charge transfer resistance at the interfaces and high frequency bulk transport resistance throughout a heating–cooling measurement cycle, showing the influence of both applied bias and temperature on these parameters. The authors postulated that by increasing the temperature to 85 °C, ion migration increased, and electro-migration accelerated because of both applied voltage and thermal effects. Furthermore, on reducing the temperature to 25 °C, both resistances increased, which was related to impeded charge transfer at the interfaces and charge transport in the bulk of perovskite because of ion accumulation at the interfaces.

With growing interest in low-bandgap, low-toxicity perovskite materials, for example, tin (Sn)-based perovskites, dark IS measurements have been employed to understand the underlying mechanisms in these PSCs. Jokar et al., extracted  $R_{rec}$  from dark IS over a bias range of 0 V to open circuit voltage ( $V_{oc}$ ) to show the impact of using a new azetidinium (AZ) cation in  $AZ_xFA_{1-x}SnI_3$  PSCs.<sup>[50]</sup> Enhancement in the  $R_{rec}$  was observed by adding 15 mol% of AZ to the  $FASnI_3$  absorber layer. Song et al., utilized dark IS to analyze the interfacial recombination between  $FASnI_3$  and indium doped tin oxide (ITO) substrate which was preheated at temperatures between 100 – 500 °C and modified by a self-assembled monolayer (SAM).<sup>[51]</sup> IS on SAM-based PSCs in the dark over a bias voltage range of 0.2–0.5 V showed highest  $R_{rec}$  values in the Nyquist plot at  $T = 400$  °C. Wang et al., reported that increased  $R_{rec}$  resulted from IS measurement under dark condition for Sn perovskite doped with  $FeCl_2$  compared to the pristine device.<sup>[52]</sup> This improvement was due to the reduction of defect states and the suppression of carrier recombination.

### 2.1.2. Capacitance Spectroscopy

Capacitance spectroscopy (CS) has emerged as a viable technique to characterize important mechanisms in PSCs such as defect-mediated recombination at the interfaces of the perovskite with corresponding charge selective layers.<sup>[53,54]</sup> Capacitance can be measured as a function of parameters such as frequency, applied bias, temperature, and time. CS provides a pathway to understand properties of perovskite films, such as—defect and doping densities, activation energy, and dielectric constant.<sup>[54,55]</sup> The frequency-dependent capacitance can be used to determine the density and energy of the trap states based on the characteristic frequency response of the latter.<sup>[53]</sup>  $C-f$  spectra typically exhibit three capacitance plateaus over low, intermediate, and high frequency ranges. The high frequency capacitance (>1 MHz) rapidly decreases with frequency due to the series resistance of the contact electrodes. The stable plateau in the mid-frequency part (1–100 kHz) is related to the geometrical capacitance ( $C_g$ ), while the low frequency capacitance (<1 kHz) may provide insights

on a myriad of phenomena, including ion migration,<sup>[54]</sup> ionic–electronic charge accumulation at the interfaces of perovskite and charge selective layers,<sup>[21,40]</sup> and charging–discharging of the Debye layers.<sup>[56,57]</sup> Generally, capacitance–voltage ( $C-V$ ) measurements are performed by applying an AC perturbation and extracting capacitance under varying voltage biases ( $\approx -1$  to 1 V).<sup>[58]</sup> The identification of depletion layer capacitance can provide information about the doping density in the absorber.<sup>[53]</sup> Furthermore, M–S analysis can be applied to  $C-V$  data, and the doping density and built-in potential can be extracted.

Temperature-dependent capacitance involves measuring the capacitance of a PSC device over a temperature range. From this measurement, the activation energy of trap states and carrier mobility in the perovskite layer can be determined. TAS is an example of capacitance measurement as a function of temperature. Capacitance can also be measured as a function of time after the application of a voltage step at various temperatures. Deep level transient spectroscopy (DLTS) is a time-dependent capacitive technique that is employed to provide information about trap distribution and trap density. Like TAS, DLTS is a temperature-sweep technique with the difference of operating in the time domain and applying a square voltage perturbation.<sup>[28,59]</sup> Due to the presence of ions in PSCs, care must be taken to measure depletion capacitance.

Capacitance as a function of temperature and time was used by McGovern et al., to study the impact of grain sizes and crystal defects on the activation energy of trap states in PSCs.<sup>[60]</sup> The authors employed transient ion drift capacitive method to understand ion migration in methylammonium lead bromide ( $MAPbBr_3$ ). In their study, capacitance was measured versus time (0–1 s) over five temperature steps (from 210 to 330 K) for small (1.7  $\mu m$ ) and large grained (11.3  $\mu m$ ) perovskite absorber layers. The activation energy was reported to increase from 0.17 to 0.28 eV with increasing grain size, which indicated that an elevated barrier for ion migration was detected for larger grained absorbers. Among the above-mentioned CS methods, M–S and TAS analyses will receive further attention in the sections below.

### 2.1.3. Mott–Schottky Analysis

For many optoelectronic applications, the Mott–Schottky (M–S) analysis is an IS-based characterization technique used for the evaluation of the charge density profile of semiconductor junctions in the dark. The M–S analysis consists in the measurement of the depletion layer capacitance ( $C_{dep}$ ) due to the change of charge occupation at the edge of the depletion zone of width ( $w$ ). This capacitance is measured at a single high frequency under reverse and low forward voltages, while minimal charge injection occurs in the device. The collected data is represented as a  $C^{-2}-V$  graph, which is commonly referred to as the M–S plot (see **Figure 3**). Various charge density profiles can be modeled in different ways, with the most classic examples summarized in **Table 2**. For constant density profiles, the M–S behaves linearly from reverse to low forward bias as  $C_{dl}^{-2} = 2(V_{bi} - V)(q\epsilon_0\epsilon_r N_{A(D)})^{-1}$ , and the curve fitting allows for the evaluation of the built-in voltage ( $V_{bi}$ ) and the concentration of acceptor ( $N_A$ ) and/or donor ( $N_D$ ) shallow defect

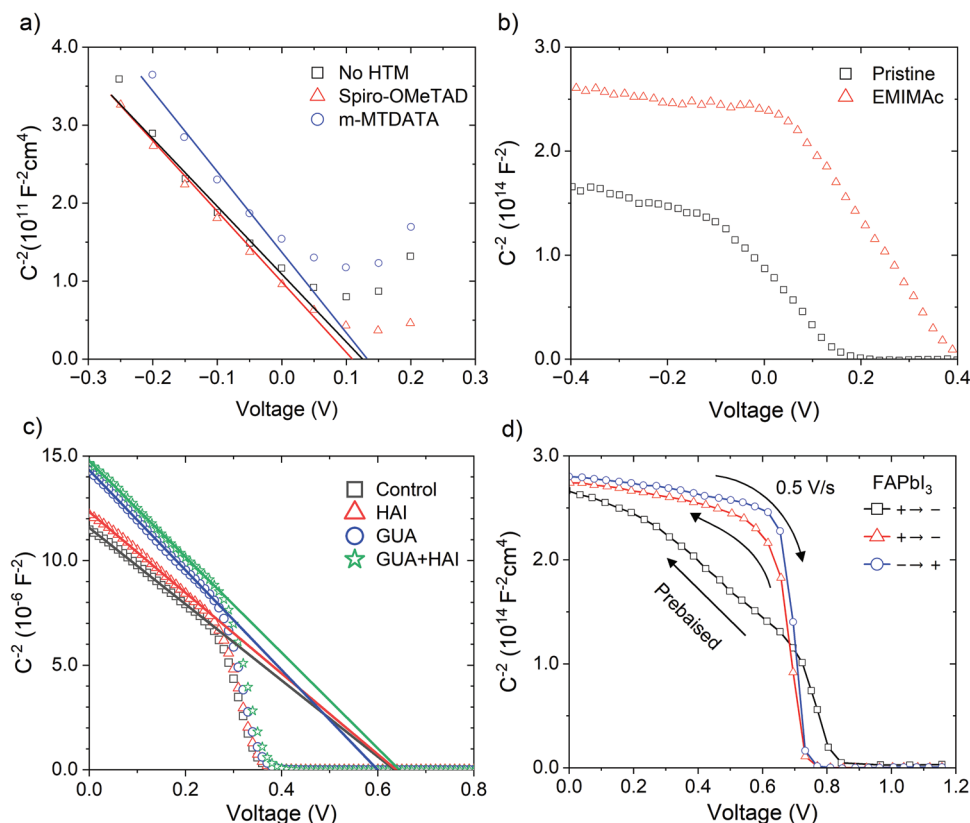


**Figure 3.** a) Mott–Schottky (M–S) plot of CsSnI<sub>3</sub> solar cell without hole transport material (HTM), and with HTMs including Spiro-OMeTAD, and 4, 4′, 4″-tris (*N,N*-phenyl-3-methylamino) triphenylamine (m-MTDATA) shows higher  $V_{bi}$  and lower charge carrier concentration for the m-MTDATA-based PSC; the solid lines used for fitting the graphs are based on the equation in the main text. Reproduced with permission.<sup>[66]</sup> Copyright 2014, Wiley Online Library. b) M–S analysis of pristine and 1-ethyl-3-methylimidazolium acetate (EMIMAc) added CsSnI<sub>3</sub> perovskites illustrating a change in charge density profile from nearly n–p to n–i–p behavior. Reproduced with permission.<sup>[67]</sup> Copyright 2022, Wiley Online Library. c) M–S plots of modified MA<sub>0.3</sub>FA<sub>0.7</sub>Pb<sub>0.5</sub>Sn<sub>0.5</sub>I<sub>3</sub> PSC devices after pre-biasing at 2 V for 1 min (M–S measurement carried out in dark at 10 kHz). Reproduced with permission.<sup>[68]</sup> Copyright 2022, American Chemical Society. d) M–S plots of a FAPbI<sub>3</sub> device showing the effect of measurement conditions with forward and backward bias sweeps, and pre-bias. Pre-bias voltage was 1.5 V applied for 20 s before the capacitance–voltage scan with a subsequent fast 500 mV s<sup>−1</sup> bias scan in reverse direction. Reproduced with permission.<sup>[27]</sup> Copyright 2018, American Chemical Society.

**Table 2.** Different charge density profile models and corresponding expressions.

Model	Depletion layer width	Capacitance M–S analysis	Ref.
Abrupt p–n homojunction	$w = \sqrt{\frac{2\epsilon_0\epsilon(N_A+N_D)}{qN_A N_D} (V_{bi}-V-2V_{th})}$	$C^{-2} = \frac{2(N_A+N_D)}{q\epsilon_0\epsilon N_A N_D} (V_{bi}-V-2V_{th})$	[63]
One-sided abrupt p–n junction ( $N_A \ll N_D$ )	$w \cong \sqrt{\frac{2\epsilon_0\epsilon}{qN_A} (V_{bi}-V)}$	$C^{-2} \cong \frac{2(V_{bi}-V)}{q\epsilon_0\epsilon N_A}$	[63]
Abrupt p–n heterojunction	$w = \sqrt{\frac{2\epsilon_0\epsilon\epsilon_D(N_A+N_D)^2}{qN_A N_D(N_A\epsilon_A+N_D\epsilon_D)} (V_{bi}-V)}$	$C^{-2} = \frac{2(N_A\epsilon_A+N_D\epsilon_D)}{q\epsilon_0 N_A\epsilon_A N_D\epsilon_D} (V_{bi}-V)$	[64]
One-side abrupt p–i–n homojunction ( $N_A \ll N_D$ )	$w = \sqrt{\frac{2\epsilon_0\epsilon}{qN_A} (V_{bi}-V) + w_i^2}$	$C^{-2} \cong \frac{2(V_{bi}-V)}{q\epsilon_0\epsilon N_A} + \left(\frac{w_i}{\epsilon\epsilon_0}\right)^2$	[63]
Abrupt p–i–n homojunction	$w = \sqrt{\frac{2\epsilon_0\epsilon(N_A+N_D)}{qN_A N_D} (V_{bi}-V) + w_i^2}$	$C^{-2} = \frac{2(N_A+N_D)}{q\epsilon_0\epsilon N_A N_D} (V_{bi}-V) + \left(\frac{w_i}{\epsilon\epsilon_0}\right)^2$	[65]
Linearly graded p–n homojunction	$w = \sqrt[3]{\frac{12\epsilon_0\epsilon}{q\alpha_p} (V_{bi}-V)}$	$C^{-3} = \frac{12(V_{bi}-V)}{q\alpha_p\epsilon_0^2\epsilon^2}$	[63]
Arbitrary doping profile p–n homojunction	$w = \frac{\epsilon_0\epsilon}{C}$	$N(w) = -\frac{2}{q\epsilon_0\epsilon} \left(\frac{\partial C^{-2}}{\partial V}\right)^{-1}$	[64]

“A” and “D” refer to the acceptor or donor side of the junction,  $N$ , the density of dopants;  $\epsilon_0$ , is the vacuum permittivity;  $\epsilon$ , the dielectric constant,  $q$ , the elementary charge;  $V_{th}$ , the thermal voltage;  $V_{bi}$  the built-in voltage; and  $\alpha_p$  is the doping concentration gradient.

levels, with  $q$  being the elementary charge and  $\epsilon_0$  the vacuum permittivity.<sup>[61,62]</sup>

Inverted planar (p-i-n) and planar (n-i-p) PSCs show a “squared” M-S plot, where the capacitance is almost constant from reverse to low forward bias before it abruptly drops towards the high injection regime.<sup>[26,28,69,70]</sup> This is the case where  $C_{\text{dep}}$  cannot be experimentally discerned from other capacitances in PSCs including chemical capacitance ( $C_{\mu}$ ), trap capacitance,  $C_g$  of different layers, and ionic capacitances in the bulk and at the interfaces. Due to overlapping timescales of the capacitance responses, it can be challenging to discern which capacitance is responding over the defined voltage range.<sup>[53]</sup> Therefore, the applicability of the M-S analysis in PSCs may not be fully justified.<sup>[26,71]</sup> Recommended analysis requires the verification of: i) the suitable AC high frequency perturbation (typically 10–40 mV for PSCs); ii) the adequate measurement frequency to elude the ionic capacitance ( $>1$  kHz for thin-films);<sup>[53]</sup> iii) the appropriate DC bias range from reverse toward forward voltage (typically  $-0.5$  to  $1$  V, but below the exponential increase due to high injection); and iv) the physical meaning of the reported doping density, that is, p- or n-type.

For PSCs under dark condition, the capacitance should ideally behave as  $C_{\text{dep}}$  considering the dielectric constant and thickness of the absorber layer, while artifacts arising from instability and mobile ions should be discarded.<sup>[26]</sup> Consequently, only a few examples can be found in the literature where the conditions for M-S analysis apply,<sup>[66,72]</sup> such as the M-S plots related to Sn-based  $\text{CsSnI}_3$  PSCs shown in Figure 3a,b, which indicates that these perovskites are homogeneously doped. In some other studies,<sup>[67,73–75]</sup> the M-S plot suggests that the modification of the tin perovskite either by additive engineering or ionic displacement increases the shallow defect concentration toward the interfaces in a way that the device is still p-i-n or n-i-p, but the intrinsic region has been thinned enough so the  $C_{\text{dep}}$  is measurable. Interestingly, for the above referenced exceptional devices, a correlation can be found between the perovskite additives including Sn and/or Cl and defect concentration.

The bias scan rate and pre-biasing was found to modify the capacitance and consequently, the shape of the M-S plots by Almora et al.<sup>[26]</sup> and Fischer et al.,<sup>[27]</sup> respectively. Specifically, pre-bias was found to produce a transition from a “squared” p-i-n like shape to a more “triangular” p-n type M-S plot. Notably, the perovskite composition seems to define the proper small ion mobility for the M-S experiment to be carried out. For instance,  $\text{MAPbI}_3$  is hardly found to respond to pre-biasing,<sup>[27]</sup> while  $\text{MA}_{0.3}\text{FA}_{0.7}\text{Pb}_{0.5}\text{Sn}_{0.5}\text{I}_3$  and  $\text{FAPbI}_3$  have been found to be affected by pre-biasing. Zhang et al., applied 2 V to an inverted  $\text{MA}_{0.3}\text{FA}_{0.7}\text{Pb}_{0.5}\text{Sn}_{0.5}\text{I}_3$ -based PSC for different periods from 0 to 120 s during M-S measurements.<sup>[68]</sup> PSCs included in the experiment were pristine  $\text{MA}_{0.3}\text{FA}_{0.7}\text{Pb}_{0.5}\text{Sn}_{0.5}\text{I}_3$  PSC,  $\beta$ -guanidinopropionic acid (GUA)-based PSC, hydrazinium iodide (HAI)-based PSC, and hybrid GUA + HAI based PSC. The authors reported that the M-S plots, for samples pre-biased at 2 V, reached a saturated state after 60 s, indicating that this timescale as optimum duration for pre-biasing in this M-S experiment (Figure 3c). Fischer et al., compared M-S plots for a  $\text{FAPbI}_3$ -based PSC in forward and reverse scan directions without pre-biasing and reverse scan with pre-biasing for 20 s at the applied voltage of 1.5 V, see Figure 3d.<sup>[27]</sup> The authors suggested that ap-

plying a large  $\bar{V}$  ( $>1$  V) prior to M-S measurements can fully revert the ion distribution and redistribute mobile ions within the bulk perovskite, which are generally accumulated at the interfaces between perovskite and charge transporting layers. This “doping redistribution” allowed for the measurement of  $C_{\text{dep}}$  by using a relatively fast reverse voltage sweep ( $0.5 \text{ V s}^{-1}$ ).

As most of the perovskite absorber layers are intrinsic in PSCs, they prevent the appropriate interpretation of M-S analysis, although pre-biasing approach to the low frequency capacitance can be used to characterize the ionic properties of the perovskites. Nonetheless, M-S analysis would only work for samples where the characteristic ionic relaxation time is not in conflict with the experimental boundaries. In general, timescales for the ionic migration in perovskites have been reported in the range of milliseconds to hours, depending on the sample and perturbation conditions.<sup>[36]</sup> After pre-biasing, only “slow ions” may therefore be characterized since “fast ions” may rapidly return from pre-bias to equilibrium conditions, resulting in either the same p-i-n graph or effects such as M-S plot hysteresis.

#### 2.1.4. Thermal Admittance Spectroscopy

Thermal Admittance Spectroscopy (TAS) refers to the analysis of IS measurements in the dark while sweeping temperature. Notably for PSCs, the temperature ranges to be covered with TAS should be within a range of stable perovskite crystal phase, for example, for  $\text{MAPbI}_3$  tetragonal phase a range from 160–330 K is advised.<sup>[76]</sup> TAS probes the  $C_{\text{dep}}$ , which suggests that this technique requires similar validation conditions as M-S analysis.<sup>[26,28]</sup> At every temperature point within the suitable range for TAS measurements, the defect distribution has a characteristic emission rate which depends on the defect density ( $N_t$ ) and the trap energy ( $E_t$ ). These values are obtained by applying the TAS formula to the  $C-f$  data for a range of temperatures.<sup>[28,77]</sup> Accordingly, many studies uses TAS for correlating device performance improvement with modifications in  $E_t$  and  $N_t$ , and/or the corresponding effective trap density of states (DOS) as a function of the demarcation energy or angular frequency, either at an interface or along the perovskite bulk.

A thin [6,6]-phenyl  $\text{C}_{61}$  butyric acid methyl ester (PCBM) layer was employed by Dong et al. to optimize the ETL interface between aluminum-doped zinc oxide (Al:ZnO) and  $\text{MAPbI}_3$  in an inverted planar device.<sup>[77]</sup> Using TAS characterization method, the authors showed that introducing the PCBM layer promoted charge extraction and passivated the interfacial defects. Subsequently, lower  $N_t \approx 5.9 \times 10^{15} \text{ cm}^{-3}$  (vs  $N_t \approx 1.8 \times 10^{16} \text{ cm}^{-3}$  for baseline devices), and  $E_t \approx 0.35 \text{ eV}$  (vs  $0.49 \text{ eV}$ ), contributed to the improvement of PCEs for PCBM interlayer-based PSCs from 13% to 17%. To reduce the  $N_t$  of the perovskite absorbers, additives are often introduced. Some additives, however, may lead to higher defect densities; for example, the excess concentration of MAI in the precursor solution was found to increase the trap density of  $\text{MAPbI}_3$  by  $\approx 50\%$ .<sup>[78]</sup> Yu et al., reported the decrease of trap states in polycrystalline  $\text{MAPbI}_{3-x}\text{Cl}_x$  perovskites as a consequence of mechanical stress.<sup>[79]</sup> The deformation and shift in GBs was reported to influence the density of defects at GBs and reduce the DOS by more than 20%. Encapsulation of PSCs in a  $\text{N}_2$ -filled glovebox and storing them in a dark condition for a few

hours was suggested as an alternate method for reducing DOS (as confirmed by TAS), specifically in shallow trap regions.<sup>[80]</sup>

Several studies employed TAS to show improved passivation and reduced  $N_t$  values by incorporating additives into the Pb-based perovskite precursor inks.<sup>[81–83]</sup> Bilateral alkylamines, has shown significant impact to enhance PCEs of MAPbI<sub>3</sub> (18.3% to 21.7%) and Cs<sub>0.05</sub>FA<sub>0.70</sub>MA<sub>0.25</sub>PbI<sub>3</sub> (17.0–21.5%)-based PSCs.<sup>[83]</sup> Accordingly, incorporating 1,3-diaminopropane (DAP) into the perovskite ink resulted in one to two orders of magnitude lower DOS for DAP-based MAPbI<sub>3</sub> than for pristine MAPbI<sub>3</sub>, as seen by TAS measurements. Li et al., reported low  $N_t$  in PSCs by the addition of SnI<sub>2</sub> and CuBr<sub>2</sub> into the Pb-based perovskite inks.<sup>[84]</sup> Using TAS measurements, a lower DOS was observed for the inverted lead–tin–copper (Pb–Sn–Cu) ternary PSCs with a PCE of 21.1% compared to the MAPbI<sub>3</sub> device. Gharibzadeh et al., performed TAS analysis to show the advantage of passivating defects at both GBs and perovskite/C<sub>60</sub> interface in a p–i–n PSC.<sup>[85]</sup> The increase in activation energy ( $E_a$ ) from 0.502 to 0.696 eV and the reduction of electron trap density from  $9.2 \times 10^{15}$  to  $3.7 \times 10^{15} \text{ cm}^{-3}$  indicated effective suppression of defects accumulated at both the GBs and the surface of the perovskite films compared to the reference device. Consequently, the operational stability was improved for the passivated PSC under illumination.

Typical defect densities and activation energies, along with the corresponding PSC efficiencies (see Table S2, Supporting Information, for additional details) derived from TAS and DLTS studies are summarized in **Figure 4a–c**. Notably, most of the studies in the literature focused on the material variations of MAPbI<sub>3</sub>, while Sn-based and Br-rich devices appear to still lack intensive characterization via TAS or DLTS at present. As seen in Figure 4a, the derived trap concentrations are mostly around  $10^{16} \text{ cm}^{-3}$  which is above the minimum concentration that can be measured by capacitive techniques,  $N_{d,\text{min}} \approx 6.75m_c k_B T \epsilon_r \epsilon_0 q^2 L^{-2}$  (here,  $m_c$  is an “ideality factor-like” capacitance parameter by Ravishankar et al.,<sup>[86]</sup> and  $k_B T$  is the thermal energy; see dotted line at  $6 \times 10^{14} \text{ cm}^{-3}$  in Figure 4a). The estimation of  $N_{d,\text{min}}$  is useful for validation and evaluation of the lower density limit measurable via capacitive techniques.

Interestingly, some of the reported defect densities may be close or even above the effective density of states at the band edges  $N_{C,V}$ , which can be estimated as a function of the effective mass  $m_{e(h)}^*$  of electrons (holes) and the thermal energy  $k_B T$ ,  $N_{C,V} = 2(2\pi m_{e(h)}^* k_B T)^{3/2} h^{-3}$ ; with  $h$  being Planck’s constant. The value of  $N_{C,V}$  (see dashed line at  $8 \times 10^{16} \text{ cm}^{-3}$  in Figure 4a) relates to the concentration of electrons (holes) that contribute to the capture/emission process to which the TAS/DLTS formalisms refer. In other words, “trap” concentrations close or above  $N_{C,V}$  may suggest the limitation of TAS/DLTS to adequately characterize the sample. Figure 4b shows the corresponding activation energies distributed between shallow and mid-gap states. In agreement to high PCEs of PSCs, shallow defects are most often found, which are known to have low to no effect on non-radiative recombination. Yet, determining the nature of the defects is challenging due to the nearly intrinsic character of the perovskite and the complications of having additional dopants/additives contributing to the capacitive signal. Interestingly, although rarely encountered, some activation ener-

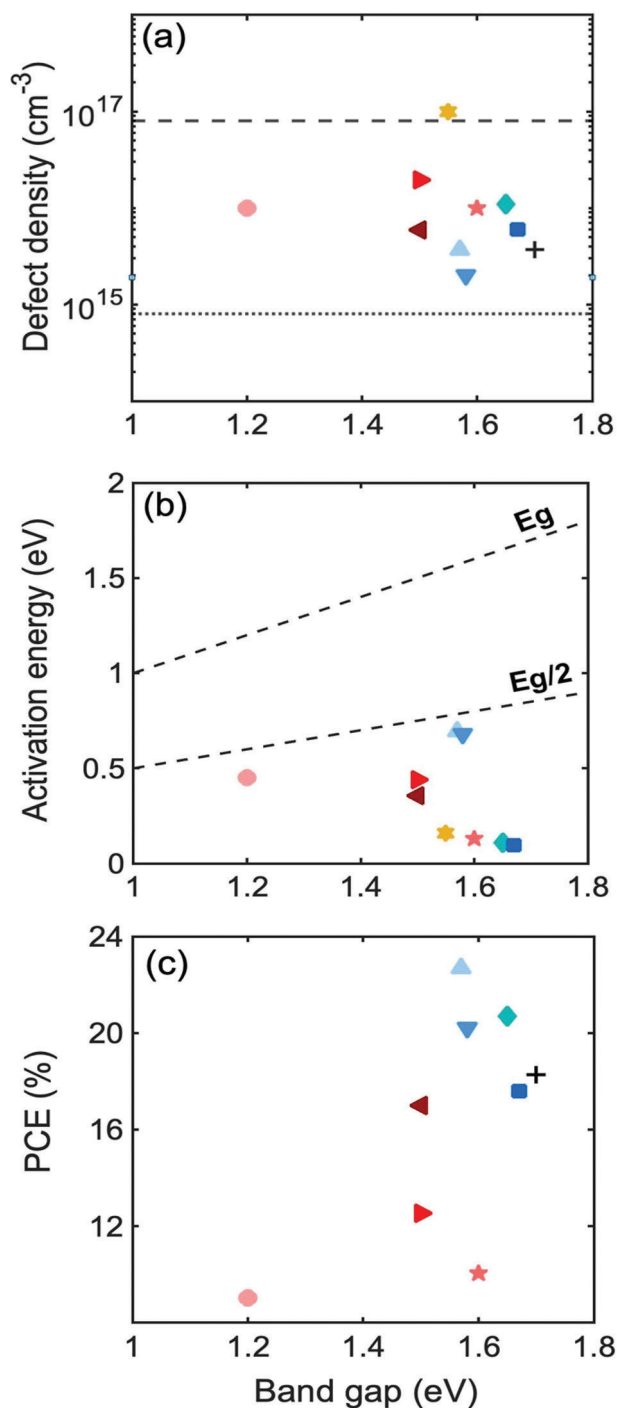


**Figure 4.** Review of a) defect density, b) activation energy, and c) power conversion efficiency versus band gap energy for PSCs with various perovskite compositions from thermal admittance spectroscopy (TAS) and deep-level transient spectroscopy (DLTS). The legend for the original publication of each report can be found in Table S2, Supporting Information. For the minimum doping density measured by capacitive methods (dotted line),  $N_{d,\text{min}}$ ,  $T = 300 \text{ K}$ ,  $m_c = 1$ ,  $\epsilon_r = 15$ , and  $L = 500 \text{ nm}$ ; and for the effective density of states (dashed line),  $N_{C,V}$ ,  $m_e^* = m_h^* = 0.1 m_0$  ( $m_0$  is the electron mass).



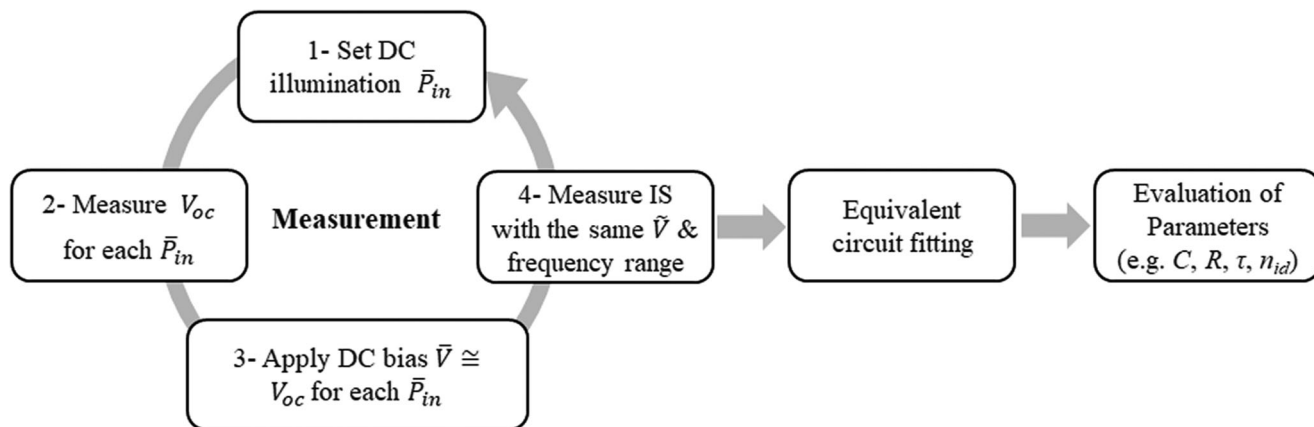


**Figure 5.** The process of open-circuit recombination analysis by impedance spectroscopy (ORIS) measurement under different light intensities at open-circuit (OC) voltage.

gies close to the mid-gap level show the higher efficiencies (see Figure 4c), despite trap energies which are closer to the mid-gap level typically yielding higher recombination rates. This raises the question of whether the estimated activation energies correspond to trap capture/emission or yet another process or effect. Here we want to mention the possibility of neutrality of the defects, however, neutral defects should not produce a sign-defined electrical response.

To summarize, conducting IS measurements in the dark should always be considered as the first characterization step for understanding photoactive materials or devices. The comprehension should start from the simplest equilibrium situation. Furthermore, dark conditions for IS measurements may limit the influence of additional challenges during measurements such as light-mediated device degradation. Dark IS characterization can provide important results in regard to charge transport and recombination resistance, doping density, built-in potential, trap density, and trap energy level. However, given that the intended operational condition for PSCs is under illumination, it is reasonable for the dark measurements to be complemented by measurements under illumination, as described in the subsequent section.

## 2.2. Open-Circuit Recombination Analysis by Impedance Spectroscopy

The open-circuit recombination analysis by impedance spectroscopy (ORIS), is one of the most common IS methods for estimating the recombination resistance and the effective recombination lifetimes which are present under DC illumination at open circuit condition in photovoltaic devices (see Figure 5). At any other “non-OC” condition the competition between charge carrier extraction and recombination hinders the identification of the respective resistances. However, in thin film perovskites, where the charge carrier diffusion length is larger than the thickness of the absorber layer, the OC condition can be set under illumination intensities whose value of  $V_{OC}$  approaches that of the  $V_{bi}$  (flat band) for making the drift and diffusion currents nearly negligible. Accordingly, it is safe to

assume that most of the IS signal is related to the recombination resistance,<sup>[87]</sup>  $R_{rec} = (dJ_{rec}/dV)^{-1}$  since the current balance is achieved between the recombination current ( $J_{rec}$ ) and the voltage-independent photogeneration. Subsequently, provided that the electronic chemical capacitance ( $C_{\mu}$ ) is measurable and much larger than the dielectric capacitance,<sup>[88]</sup> the recombination lifetime can be extracted as  $\tau_{rec} = R_{rec} C_{\mu}$ .  $C_{\mu}$  arises due to the shift in the Fermi level energies with respect to the band edges as a result of charge carrier injection. It explains charge carrier accumulation in the perovskite layer and charging/discharging mechanisms within the device during operation.<sup>[54]</sup>

For  $V_{OC}$  values close to the  $V_{bi}$ , the resistances are almost exclusively related to recombination phenomena. However, under low illumination intensities/voltages, resistances are governed by prevalent shunt/photo-shunt processes rather than by illumination intensities or voltages. As for the capacitances, the high frequency capacitance in PSCs is attributed to the bulk dielectric polarization and typically shows a well-defined plateau in the Bode plot corresponding to the geometrical capacitance under illumination condition. Alternatively, at low frequencies, a very large capacitance is observed under illumination which increases exponentially.<sup>[89]</sup> While still debated, the origin of the low frequency resistance and capacitance has been commonly related to ionic motion and interface mechanisms. Ripolles et al., used ORIS to analyze the interface treatment in single-cation and double-cation PSCs.<sup>[90]</sup> A very low concentration of phenylethyl ammonium iodide (PEAI) salt (0.0002–0.012 M) was added during the antisolvent step in device fabrication to passivate interfacial vacancies and improve moisture stability. IS measurements were performed at  $V_{OC}$  under 1 Sun illumination for PSCs with and without PEA. The results showed lower high frequency resistance or improved transport for the devices with PEA due to the presence of PEA<sup>+</sup> cations at the grain boundaries which improved moisture resistance.

Subsequently, by reducing the recombination rate, efficiencies increased by 18%, 32%, and 4% for PEA-based MAPbI<sub>3</sub>, MA<sub>0.9</sub>Cs<sub>0.1</sub>PbI<sub>3</sub>, and MA<sub>0.5</sub>FA<sub>0.5</sub>PbI<sub>3</sub> devices, compared to the pristine device.

The determination of the  $n_{id}$ ,<sup>[29,91]</sup> from ORIS data can also be used to identify main recombination mechanisms in PSCs. In

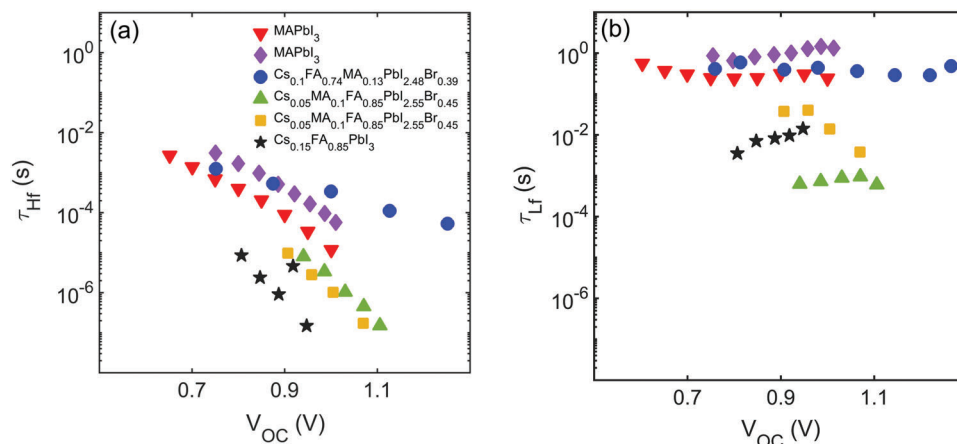


**Figure 6.** a) The high frequency and b) low frequency characteristic response times measured over a range of OC voltages for different PSC materials and configurations. The graphs show the exponential decrease of  $\tau_{Hf}$  and approximately constant behavior of  $\tau_{Lf}$  for different perovskite compositions.

this experiment, the  $n_{id}$  is obtained from the exponential slope of the high frequency resistance versus  $V_{OC}$  under different illumination intensities. In comparison to other methods, such as considering the short circuit current density ( $J_{SC}$ ) versus  $V_{OC}$  or the dark  $J$ - $V$  curve, ORIS provides a hysteresis-free assessment and separation between the electronic- and mobile ion-related recombination features.<sup>[91–93]</sup> In 2023, Bennett et al.<sup>[94]</sup> proposed analytical and numerical modeling that suggest the ideality factor  $n_{Hf}$  from  $R_{Hf}$  as an electronic (ion-migration-effect free) parameter while the ideality factor  $n_{Lf}$  from  $R_{Lf}$  comprises the recombination mode linked to the mobile ion properties. Moreover, here we stress the use of ORIS for either extracting ideality factors and/or to directly observe  $R_{rec}$ , which may find application for elucidating  $V_{OC}$  trends of devices (as from the  $J$ - $V$  curve). This is not only because of neglecting hysteresis issues but also because of the exploration of the capacitive features that may induce modifications in the density of states.

Evaluating the characteristic response time ( $\tau$ ) from the ORIS method is another approach used to obtain information on recombination mechanisms.<sup>[23,29]</sup> From the combination of capacitances and resistances, the  $\tau = RC$  can be assessed. It is pertinent to note that  $\tau$  may also include contribution from dielectric relaxation  $\tau_d = R_{rec} C_d$  of the dielectric capacitance  $C_d$ , which is the most likely situation for PSCs. For example, assuming ( $\tau = \tau_{rec} + \tau_d$ ),<sup>[88]</sup> the condition of  $C_d \ll C_\mu$  is necessary for the interpretation of  $\tau \cong \tau_{rec}$  and evidence of this has already been found in silicon,<sup>[25]</sup> organic,<sup>[95]</sup> and dye-sensitized,<sup>[87]</sup> solar cells. **Figure 6** shows high and low frequency characteristic times over a wide  $V_{OC}$  range for different PSC configurations, as summarized in Table S3, Supporting Information.<sup>[23]</sup> Each main capacitance is generally associated with a time constant. At high frequencies,  $C_g$  of the PSC and  $R_{Hf}$  would most commonly be coupled; although depending on the device and the EC model, the  $C_g$  could also include its discharge throughout the  $R_{Lf}$ . Either way, since the high frequency capacitance typically remains constant and the high frequency resistance decreases with illumination, the  $R_{Hf} C_{Hf}$  product would result in an exponential decrease in the  $\tau_{Hf} \propto \exp[-qV_{oc}/n_{\tau_{Hf}} k_B T]$ , as illustrated in Figure 6a. Higher values for  $\tau_{Hf}$  and values close to unity for high

frequency lifetime-related ideality factors  $n_{\tau_{Hf}}$  are ideal. However, at low frequencies, the capacitance  $C_{Lf} \propto \exp[qV_{oc}/n_{C_{Lf}} k_B T]$  and resistance  $R_{Lf} \propto \exp[-qV_{oc}/n_{R_{Lf}} k_B T]$  exponentially increase and decrease with illumination, respectively. Most commonly, the exponential trends are the same ( $n_{C_{Lf}} \approx n_{R_{Lf}}$ ) resulting in relatively constant low frequency characteristic time  $\tau_{Lf}$ , as shown in Figure 6b.

Markedly, the  $\tau$  values from ORIS have been compared with those measured via transient photovoltage (TPV) in organic,<sup>[96]</sup> and dye-sensitized solar cells,<sup>[97]</sup> where both theory and experiment suggest agreement between the two techniques. In PSCs, on the other hand, some studies have also found this experimental agreement between  $\tau_{Hf} = R_{Hf} C_g$  from ORIS and  $\tau$  from TPV,<sup>[23,98]</sup> which suggests a correlation between  $\tau_{Hf}$  and the recombination properties of PSCs. However, the apparent disconnection between  $\tau_{Hf}$  and  $C_\mu$  raises the question whether  $\tau$  from TPV is not a recombination lifetime and/or whether a different theoretical framework is necessary for interpreting the physical meaning of  $\tau_{Hf}$  from ORIS. Nonetheless, we highlight that this agreement between the two techniques has been found to occur only for a given  $V_{OC}$  range because IS and TPV perform better in terms of signal quality for higher and lower values of  $\bar{P}_{in}$ , respectively, and match well in intermediate illumination ranges.<sup>[23]</sup>

In summary, impedance spectroscopy analysis at quasi-open-circuit conditions can be useful in identifying the recombination mechanisms at interfaces and in the bulk. Particularly, the ideality factor from the slope of the resistance versus  $V_{OC}$  curve measured under different illumination intensities, is an effective tool that not only indicates the dominant recombination mechanisms in the device but also suggests a discrimination between the features affected by the ion migration and those that are not. Nevertheless, care must be taken when straightforwardly assuming the presence and/or absence of fundamental quantities such as the recombination and transport resistances and the chemical capacitance. There still is debate on the physical origin of several phenomena such as the exponential increase of the low frequency capacitance and the nearly constant behavior of the low frequency characteristic time with respect to the illumination intensity and thus the  $V_{OC}$ .

### 2.3. Equivalent Circuit-Oriented Impedance Spectroscopy Analyses

Equivalent circuit-oriented impedance spectroscopy (ECIS) parameterization has been exhaustively reviewed in a recent work by Guerrero et al.,<sup>[40]</sup> who also provided more general considerations for the IS characterization of PSCs. Building on this work, we not only want to provide an update on the most recent reports in this area, but also want to focus our analyses from the perspective of the IS measurement protocol and its relation to the EC modeling.

Nyquist and Bode graphs are the two main representations used not only to visualize the impedance response but also as a first approach for signal processing. The next most typical method is to use ECs to simulate the IS data by including resistive, capacitive, inductive, etc. elements in the circuit.<sup>[99]</sup> Resistors in ECs represent the reduction of current flow and dissipation of electrical energy as heat. The physical origins of resistances in ECs are manifold and include transport, charge transfer, and recombination of electronic and ionic charge carriers. Capacitors in ECs are ideal components that store electric charge. Their presence in the device can be due to the polarization of bulk and interfaces or a change in the electrochemical potential caused by local rearrangement of charge.<sup>[36]</sup> Instead of ideal capacitors ( $Z_C = 1/j\omega C$ ), constant phase elements (CPE)s ( $Z_{CPE} = 1/Q(j\omega)^n$ ,  $0 < n \leq 1$ ) can be employed to obtain better fitting, with CPE becoming an ideal capacitor for  $n = 1$ .<sup>[100,101]</sup>

ECs can quantitatively explain the dynamical mechanisms taking place in the PSC and can be relatively basic like a simple parallel RC Voigt element or more complex such as a ladder/matryoshka configuration.<sup>[100,102,103]</sup> The complexity of the circuits depends on the perovskite composition, the types of charge carrier layers, and the PSC structure itself. In addition, the utilization of each EC element should be understood in the broader context of the IS signal nature. For example, the inclusion of capacitors and inductors does not necessarily imply the presence of physical phenomena that traditionally relate to the ideal elements for energy storage in an electric or magnetic field, respectively. Instead, other phenomena can be the cause of a similar current phase-shift with respect to the voltage perturbation and tangled origins of the IS spectrum can even produce apparently anomalous outcomes, such as negative capacitances.

Importantly, even though one can always numerically find many EC models that fit the experimental data nearly perfectly with up to  $N - 1$  parameters ( $N$  is the number of experimental points), it does not mean that these mathematical parameterizations imply realistic physical meaning. Thus, for an EC to be physically validated, it should follow the principles of: i) accuracy, ii) physical representativeness, and iii) generality. The first principle is quite straightforward, and one can easily find relative and statistic error indicators in most of the signal processing fitting software. However, the balance between accuracy and physical meaning is important. In other words, a 90% accurate fit with representativeness and generality may be preferred over a 99% accurate fit for which the physical meaning is unclear.

The physical representativeness of the EC model relies on how well it describes the specific system under consideration. For instance, series connection of  $R$ - $C$  couples is a suitable description

for thick samples such as silicon solar cells,<sup>[104]</sup> where a macroscopic distribution of voltage drop is well defined; the total  $C_g$  is overlapped by  $C_{dep}$  and the quasi-neutral region may behave like a “wire” connecting in series the junction-, the contact- and/or the bulk-related processes. However, the above conditions are not generally present in thin film systems, which makes the ladder/matryoshka EC models more suitable.<sup>[100]</sup> Furthermore, the representativeness is also a function of the measurement condition. For instance, EC for quasi-open-circuit conditions should contain the most detailed description for dielectric capacitive elements, whereas the situation of significant current flow may include inductive elements.

The generality principle is one of the most critical principles in terms of validation. The EC model should not only describe a given system at a given condition but should also show coherency over a range of conditions and upon modification of the system. The simplest manifestation of the generality principle is related to the frequency range: an EC circuit should cover the simplified DC circuit toward low frequency. For instance, by using uncoupled capacitors (without parallel resistor) the current throughout all the elements in series at DC condition is disabled. Likewise, care should be given to any resistors in series with uncoupled capacitors since these elements would behave differently in AC and DC conditions. Moreover, not only does the frequency require generality from EC circuits, but also any other parameter defining the device condition, such as the DC bias and illumination. For instance, an EC model designed for ORIS protocol to be performed on a PSC should describe the same PSC at short-circuit under different illumination intensities or in the dark at different biases, either without any modifications or by being modified for each measurement condition as a particular case of a more general circuit.

In this section, several recent EC-based recent studies are showcased as examples of the three principles of EC modeling. The cell architectures, the impedance responses, and their related ECs for all the following examples are summarized in Table S4, Supporting Information. The suggested EC for a common cell structure of Glass/FTO/TiO<sub>2</sub>/MAPbI<sub>3</sub>/Spiro-OMeTAD/Au is discussed first and will be followed by examples of more complex circuits. In 2015, Pascoe et al., studied three different planar PSC configurations and measured impedance under illumination at OC to compare the behavior of different architectures.<sup>[105]</sup> The impedance response in **Figure 7a** shows two distinct features at low and high frequencies corresponding to dielectric relaxation and charge recombination at the interfaces of the perovskite layer and the adjacent contacts, respectively.<sup>[105,106]</sup> The Debye dielectric relaxation components in the EC of **Figure 7a** ( $R_2$  and  $C_2$ ) were reported to be related to the frequency dependence of the perovskite polarization.<sup>[18]</sup> Besides,  $R_1$  and contact capacitance ( $C_1$ ) were associated to the buildup of charges at the perovskite layer and its neighboring contact interfaces. Aranda et al., used IS measurement in dark condition to study HTL-free MAPbBr<sub>3</sub> devices.<sup>[89]</sup> The EC in **Figure 7b** was used to fit the impedance spectra with two arcs and three capacitances; with  $R_{HF} = R_3$  describing the conductivity of the perovskite layer and recombination processes and the IF and LF features related to the interfaces of the perovskite with the external contacts. However, the coupling between  $R_1C_1$  and  $R_2C_2$  led to one arc in the Nyquist plot and two capacitances in the  $C$ - $f$  plot. To show the impact of

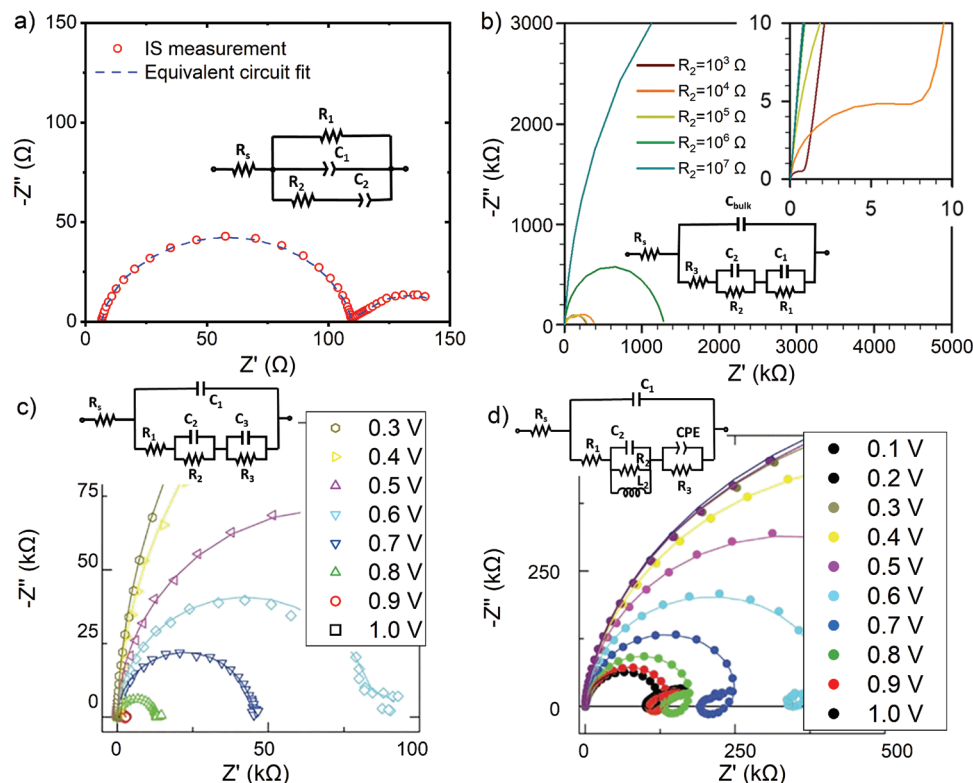


**Figure 7.** a) Nyquist plot measured for Glass/FTO/TiO<sub>2</sub>/MAPbI<sub>3</sub>/Spiro-OMeTAD/Au under open-circuit conditions at illumination intensity of 273 W m<sup>-2</sup>. Reproduced with permission.<sup>[105]</sup> Copyright 2015, American Chemical Society. b) Simulated IS data for Glass/FTO/c-TiO<sub>2</sub>/m-TiO<sub>2</sub>/MAPbBr<sub>3</sub>/Au in the dark with modification of  $R_2$  at  $R_s = 20 \Omega$ ,  $R_3 = 1000 \Omega$ ,  $C_{\text{bulk}} = 2 \times 10^{-8} \text{ F}$ ,  $R_1 = 2.8 \times 10^5 \Omega$ ,  $C_1 = 2 \times 10^{-6} \text{ F}$ ,  $C_2 = 2 \times 10^{-7} \text{ F}$ . Reproduced with permission.<sup>[89]</sup> Copyright 2019, The American Institute of Physics. c) FTO/SnO<sub>2</sub>/MAPbI<sub>3</sub>/PTAA/Au in the dark at different biases under vacuum; and d) FTO/SnO<sub>2</sub>/MAPbI<sub>3</sub>/Spiro-OMeTAD/Au measured in the dark at different biases. Reproduced with permission.<sup>[22]</sup> Copyright 2019, American Chemical Society. The equivalent circuits in the insets used for fitting the impedance responses.

individual circuit elements on the impedance response, the authors simulated IS data by varying values of circuit elements including the contact resistance,  $R_2$ , from 1 to 10<sup>4</sup> kΩ with other parameters fixed. As it is shown in Figure 7b, for certain values of  $R_2$ , two arcs in the Nyquist plot were observable, compatible with their observed data.

Sangwan et al., explored two different HTMs including PTAA and Spiro-OMeTAD in a planar PSC device by IS analysis in the dark at different forward biases.<sup>[22]</sup> The impedance spectra were modeled using three parallel  $R$ - $C$  circuits for both PTAA (shown in Figure 7c) and Spiro-OMeTAD-based PSC devices as well as an additional inductance for the PSC with Spiro-OMeTAD and efficiency of 11.9% (moderate PCE). The  $R_1$ ,  $C_1$  and the  $R_s$  represent the high frequency behavior while the two other additional  $R$ - $C$  branches were attributed to the interfacial behavior at low and intermediate frequency regions. The addition of an inductance for the Spiro-OMeTAD-based sample in Figure 7d was reasoned by the inductive loop at low frequency. Ahmad et al., performed IS for an HTL-free double mesoporous PSC including mesoporous-(m-TiO<sub>2</sub>) and m-ZrO<sub>2</sub> in the dark at multiple biases.<sup>[102]</sup> An EC with three  $R$ - $C$  branches was used to model the impedance result at low and high applied biases. The high frequency arc can be related to the counter electrode/perovskite interface and the low frequency one may be assigned to the recombination process at the TiO<sub>2</sub>/perovskite interface.

In the following article, IS measurements were performed in the dark under short-circuit conditions to ensure the stability of a triple cation 3D ((FA<sub>0.83</sub>MA<sub>0.17</sub>)Cs<sub>0.05</sub>)Pb(I<sub>0.83</sub>Br<sub>0.17</sub>)<sub>3</sub>) and 2D(PEAI)/3D PSCs during the measurement.<sup>[99]</sup> A circuit including the Bisquert transmission line (BTO) was used to better fit the low frequency response of 2D/3D PSCs and describe the giant dielectric effect at low frequencies. The high frequency response, on the contrary, was modeled using resistances and capacitances with an inductor for better fitting. The details of the structure, Nyquist plots and circuit elements can be found in Table S4, Supporting Information. Yuan et al., have shown that incorporating additives, such as cesium acetate (CsAc) into the FA<sub>0.85</sub>MA<sub>0.15</sub>PbI<sub>3</sub> perovskite precursor solution can improve PCE as well as the stability of the PSC.<sup>[107]</sup> In this work, IS measurements in the dark at a DC bias indicated improved carrier transport and lower carrier recombination rates for CsAc-based perovskite than its pristine counterpart.

Another method for improving the robustness and charge transfer of PSCs, presented by Jeong et al., is fluorinating Spiro-OMeTAD in FAPbI<sub>3</sub> PSC.<sup>[108]</sup> In this work, IS was performed at a DC bias of -1 V at times of 0, 200, and 500 h. The results illustrated enhanced stability and reduced charge transfer resistance for the fluorinated HTM-based PSC compared to the reference sample based on undoped Spiro-OMeTAD. With respect to ETLs for PSCs fabrication, SnO<sub>2</sub> has received growing

attention over  $\text{TiO}_2$  owing to its superior characteristics such as having a more suitable band energy alignment with the perovskite layer and higher electron mobility. Yang et al., complexed ethylene diamine tetra-acetic acid (EDTA) with  $\text{SnO}_2$  in a normal planar  $\text{FA}_{0.95}\text{Cs}_{0.05}\text{PbI}_3$  PSC.<sup>[109]</sup> The results of IS show smaller  $R_{\text{tr}}$  and larger  $R_{\text{rec}}$  for PSCs incorporating both EDTA and  $\text{SnO}_2$  ( $\text{E-SnO}_2$ ) compared to samples with just  $\text{SnO}_2$  or EDTA. Additionally, a hybrid layer of amorphous sol-gel  $\text{SnO}_2$  and crystalline  $\text{SnO}_2$  nanoparticles ( $\text{Bi-SnO}_2$ ) as the ETL in a planar  $\text{Cs}_{0.05}(\text{FAPbI}_3)_{0.85}(\text{MAPbBr}_3)_{0.15}$  PSC structure resulted in better band alignment with the perovskite absorber layer and lower surface defects than either of these layers separately.<sup>[110]</sup> The IS measurement carried out in the dark at a bias of 0.9 V indicated two visible arcs at lower frequencies related to the interfacial recombinations at ETL/perovskite and the bilayer interface, and an arc at high frequency associated with charge transfer resistance for the PSC based on  $\text{Bi-SnO}_2$  (Table S4, Supporting Information).

Recently, an approach was suggested in response to ambiguous interpretation of IS in different PSC devices. Hauff et al., suggested a general equivalent circuit which separates fast electrical processes (high frequency responses) from slow dynamics (low frequency responses) such as ion movements.<sup>[36]</sup> With the proposed circuit which was comprised of a series connection of a low frequency element and the high frequency features, the authors were able to comprehensively explain the high frequency component. However, a linear circuit was suggested for the low frequency branch that can be composed of different features in the spectrum depending on the various PSC architectures and measurement conditions.

In summary, the ECs reviewed here can be categorized in three different measurement conditions including: i) in dark at either different forward biases or a single bias; ii) under illumination at OC condition; and iii) in dark at short circuit (SC) condition. Three arcs in the Nyquist plots, corresponding to three  $R$ - $C$  branches in the ECs, are commonly reported for IS characterization of mixed ion/cation perovskite-based devices. To follow the generality principle, it is recommended to measure IS over a broad range of bias voltages. Negative tails or inductive loops at low frequency were also illustrated. These complex features in the Nyquist plot can be modeled using  $R$ - $L$  elements or common  $R$ - $C$  branches with negative values for  $R$  and  $C$ .

Beyond the application of classical IS protocols (Table 1), the in-depth characterization of PSCs and photovoltaics has seen significant progress in recent years. For example, DD modeling was recently used to interpret various physical behavior such as charge generation, transport, recombination, and collection in the impedance response.<sup>[57,111–113]</sup> The complex electronic-ionic behavior and chemical instability of PSCs and the lack of full understanding behind the physical behavior of some EC elements, suggest the need for alternative methods for interpreting impedance responses.<sup>[57]</sup> As a result, some groups have employed DD models in an attempt to correlate the IS with more fundamental properties, such as the charge carrier recombination rates and mobilities.<sup>[40]</sup> Ideally, complementing DD numerical simulations with EC theory analyses should provide deeper insight into the transport phenomena. Yet another complementary method to IS is LIMIS, which is achieved by applying a small light perturbation and is defined as the ratio between IMVS and

IMPS responsivities.<sup>[23,114]</sup> Both topics will be further elucidated in the following two sections.

### 3. Drift-Diffusion Modeling of IS Spectra

The equivalent circuit modeling is advantageous due to its simplicity and easy convergence during the simulation of impedance spectra, and it generally includes a combination of resistors and capacitors (at least two  $R$ - $C$  elements per PSCs). It is important to discern the physical meaning and analytical expressions for each capacitive and resistive element which can be used to evaluate more fundamental transport and materials properties such as charge carrier mobility, dielectric constants, doping and defect densities, recombination rates, and equilibrium concentrations. However, such analytical expressions are often scarce, if not missing, in EC modeling and the analytical formulae for capacitive and resistive elements are limited to rather effective approximations due to the many simplifications and assumptions needed for their deduction. Complicating things further, the presence of slow-moving ions in the perovskite layer may even add additional elements, such as inductances to the ECs.<sup>[93]</sup>

To reduce the ambiguity in the physical interpretation of circuit elements in PSC equivalent circuits, drift-diffusion (DD) modeling is employed as a more fundamental way for understanding the impedance responses and predicting the behavior of the devices based on their physical properties, although it has not been used for fitting the impedance spectra to date. Thus, DD simulations can be used as an alternative and/or a complement to EC models to numerically solve the transport equations to obtain information on transport and material properties. In DD modeling, a fully coupled set of time-dependent continuity equations and Poisson's equation can simulate transient optoelectronic measurements. For decades, the numerical tools for the mostly stationary DD solutions have been well developed for devices composed by classic inorganic semiconductors,<sup>[115–118]</sup> and organic materials.<sup>[95,119]</sup> Further developments have also been achieved for the simulation of transient techniques as well as impedance spectroscopy.<sup>[111,112,120,121]</sup> This approach not only provides a direct estimation of the basic transport parameters but can also be combined with the EC models to discern the meaning of the resistive and capacitive elements in semiconductor devices such as PSCs. The emergence of PSCs required the inclusion of the time dependency and the dual electronic-ionic conductivity with a primary focus on the hysteresis phenomena of the  $J$ - $V$  curve.<sup>[122–129]</sup>

There are several simulators with the capability of DD modeling in solar cells such as Driffusion (open source),<sup>[112,130]</sup> IonMonger (open source),<sup>[128,131]</sup> SCAPS,<sup>[115]</sup> SILVACO,<sup>[132]</sup> ASA,<sup>[116]</sup> and SETFOS.<sup>[133–136]</sup> Table S5, Supporting Information, compares these simulators in terms of numerical method, boundary conditions, assumptions, the number of charge carrier species, and measured parameters. Some examples of employing these simulators for DD modeling of impedance response in PSCs are discussed in this section.<sup>[112,137]</sup>

Among these simulators, Driffusion and IonMonger have been mostly employed for simulating the impedance response for PSCs. This open-source software use the solution of the charge and electrostatic concentration profiles of the device under steady-state conditions as initial conditions for the transient simulation at each frequency. The impedance response is

simulated over all frequencies with input of key parameters, such as the ones listed in Table S5, Supporting Information. A key difference between Driffusion and IonMonger is the employed method for simulating the interfaces between two dissimilar layers. Driffusion considers a discrete interlayer interface to have a smooth transition in material properties, while IonMonger is based on an abrupt interface model.<sup>[130,131]</sup>

Illustratively, the low frequency capacitance in the IS spectra was interpreted based on the ionic DD model by Jacobs et al.,<sup>[111]</sup> The authors considered mobile ion densities alongside electron and hole populations (for **Figure 8a**,  $N_A - N_D = 4 \times 10^{17} \text{ cm}^{-3}$ ,  $N_{\text{ion}} = 1 \times 10^{18} \text{ cm}^{-3}$ , for additional values for the initial parameters see Table S6, Supporting Information) with the critical distinction that ions can only move within the perovskite layer. In all the simulations, at least two ionic charge distributions were utilized and mechanisms like ionic generation–recombination and interaction between ions and charge carriers were not considered. As a result, the slow response of mobile ions to the external applied potential was suggested as the reason for the giant capacitance as well as some other features including inductive loops and negative capacitances in the low frequency region. **Figure 8a** shows the simulated IS spectra featuring an inductive loop and the enhancement of the high frequency arc with ETL doping ( $N_b$ ) and interfacial defect densities ( $D_{\text{it}}$ ). **Figure 8b** represents the Nyquist plots simulated under dark condition at 1.0 V forward bias for different bulk Shockley–Read–Hall (SRH) defect densities ( $N_b$ ) and surface recombination velocities ( $V_r$ ). The figure shows the sign of the capacitance in dependence on  $N_b$  and  $V_r$ . Therefore, SRH recombination led to negative capacitance while surface recombination resulted in positive capacitance.<sup>[111]</sup>

The low frequency features in the IS spectra were also explored by Moia et al., using a DD model.<sup>[112]</sup> This model, based on the open-source simulation tool Driffusion, assumes a higher concentration of mobile ions than electronic charge concentration and a higher conductivity of bulk electronic than the ionic conductivity under operation. Moreover, in this simulation, only one defect species is mobile. With these assumptions, the large low frequency capacitance and inductive behavior were explained by coupling interfacial electronic charge transfer and ionic redistribution without the accumulation of electronic charges at the interfaces of perovskite with charge transporting layers. **Figure 8c,d** shows Nyquist and  $C-f$  plots simulated by the DD model around  $V_{\text{OC}}$  at different light intensities. The values of the simulation parameters can be found in Table S6, Supporting Information. Later, Miyano et al., used the proposed method in ref. [112] to explore the superior impact of ionic motion on the opto-electronic properties and operational stability of PSCs.<sup>[138]</sup> They also revised the IS interpretation of some published data by including the influence of ionic motion.

A DD model including mobile ions and charge traps was employed in another study by Neukom et al., to describe the experimental results in the steady-state, transient, and frequency domain.<sup>[136]</sup> The authors used SETFOS and also transfer matrix method to calculate charge generation profile within the perovskite layer. The experiments were performed both in the dark and under illumination on vacuum deposited inverted MAPbI<sub>3</sub> PSCs. Notably, this model was the first to combine steady-state, transient, and frequency-domain in both simulations and mea-

surements, instead of presenting a single experimental method while being able to explain several phenomena like  $J-V$  curves with hysteresis. While the focus of the studies presented thus far was on the low frequency response, the faster electronic signal for frequencies above 10 kHz can also be of interest.

The high frequency IS response was interpreted by Riquelme et al.,<sup>[57,137]</sup> who used the open-source simulation tool IonMonger.<sup>[127]</sup> The values of the simulation parameters are listed in Table S6, Supporting Information. In this simulation, SRH and/or bimolecular recombination mechanisms were considered in the bulk, while, at the interfaces, only SRH recombination was assumed. Besides, the selective transport layers were assumed to be highly doped, meaning that the conduction (valence) band energy in the ETL (HTL) was considered to be equal to the Fermi level in that layer. Apart from the electrons and holes, the impact of positive anion vacancies was considered as well. In addition, the key properties such as recombination and charge collection were extracted from the impedance response to understand the steady-state operation. Furthermore, using bulk recombination as well as slow ionic motion in the DD model, the impedance response of some features like high frequency flat capacitance, low frequency negative capacitance and inductive loops were reproduced. **Figure 8e,f** shows the DD simulated impedance spectra at OC and varied illumination intensities. The size of the low frequency arc in **Figure 8e** remained unchanged while the high frequency arc decreased with illumination. The frequency plot in **Figure 8f** shows the enhancement of the characteristic frequency in the high frequency part by illumination whereas the characteristic frequency in the low frequency section stayed unchanged. In another work by Riquelme et al., DD modeling was used for physical interpretation of the elements of two common equivalent circuits including series and parallel  $R-C$  branches, respectively.<sup>[139]</sup> The results show that the high frequency resistance contains information about the electronic recombination processes and can be utilized to evaluate  $n_{\text{id}}$  and carrier collection efficiency.

In an interesting study by Bennett et al., a model was proposed which directly compared the analytical result based on the underlying DD model of charge carrier density and ion vacancy motion, with the experimental IS response without performing time-consuming simulations.<sup>[93]</sup> This fully coupled ionic–electronic DD model was used for a planar PSC, which considered only one positive ion vacancy species and mobile charge carriers in the bulk of perovskite. What makes this work different from others is that the authors proposed a physics-based analytical model with some approximations based on the surface polarization model (SPM) and Boltzmann distribution throughout the device. This model was employed to simplify the DD formalisms when analyzing the low frequency impedance response, which was in accord with the analytic and the DD model close to OC voltage. The SPM which was proposed by Bisquert et al., is based on the delayed response of surface potential ( $V_s$ ), created by ionic accumulation at the ETL/perovskite interface, due to variations of an external voltage ( $V$ ). As a result, higher recombination rate and negative capacitance are expected due to the accumulation of ions at the perovskite surface.<sup>[10,21]</sup>

To summarize, several features in the impedance response of PSCs including the flat high frequency capacitance, the large low frequency capacitance, negative capacitance, and

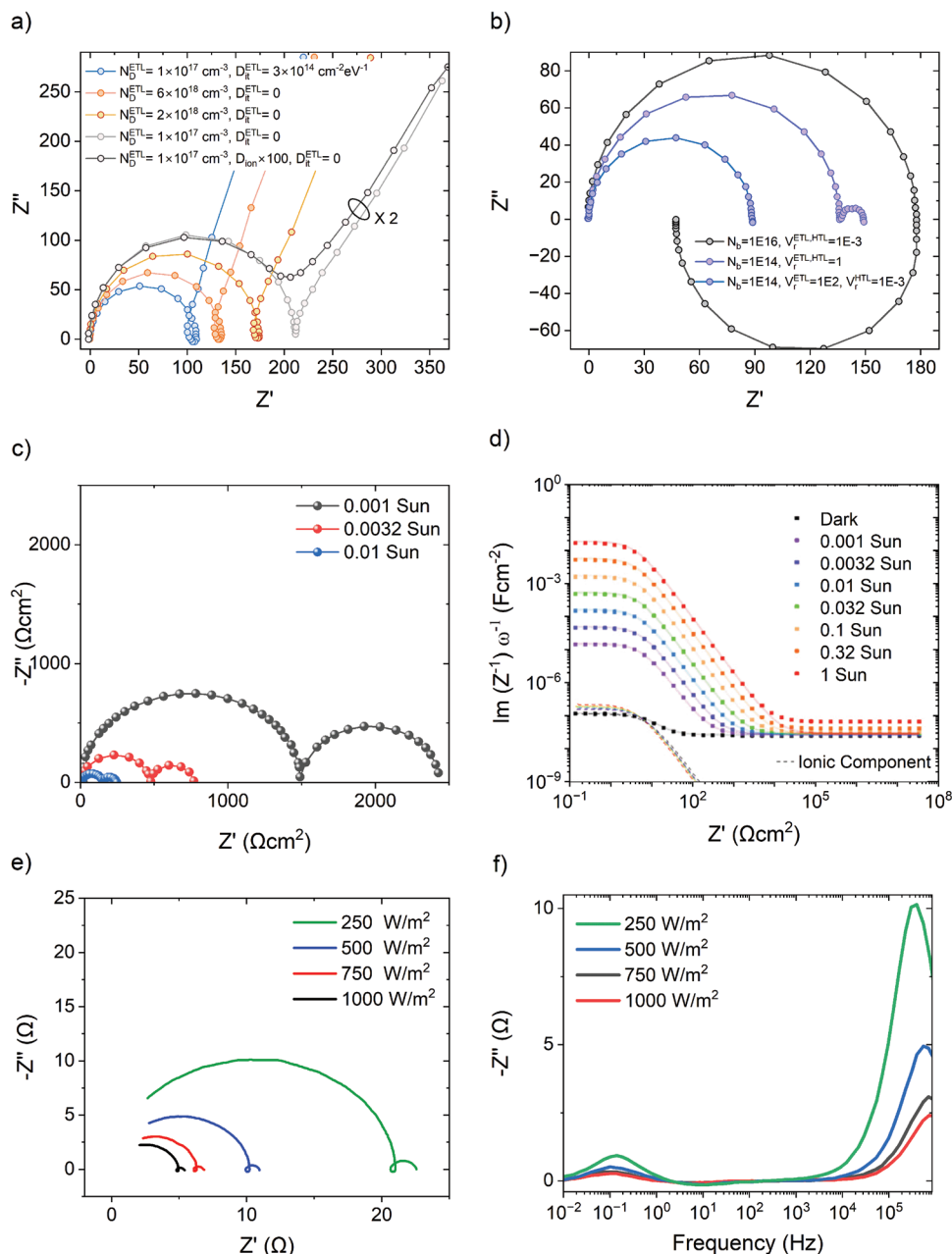


**Figure 8.** Simulated Nyquist plots a) under illumination at 0.6 V for different  $N_D$  and  $D_{it}$  show a significant change in the size of the high frequency time constant and a disappeared inductive loop for the fast ion migration (The data in gray and black were scaled down by a factor of two for visibility), b) under dark condition at 1.0 V forward bias for different bulk recombination defect densities and surface recombination velocities. Reproduced with permission.<sup>[111]</sup> Copyright 2018, American Institute of Physics. c,d) Simulated Nyquist plot and capacitance,  $\omega^{-1} \text{Im}(z^{-1})$ , versus frequency of a p-i-n device containing mobile ionic charges using drift-diffusion (DD) simulation around  $V_{OC}$  under illumination with a voltage perturbation of 20 mV, respectively. The dashed line in (d) indicates the simulated ionic capacitance. Reproduced with permission.<sup>[112]</sup> Copyright 2019, Royal Society of Chemistry. A DD simulated device under varied illumination intensities at OC shows e) the reduction of the high frequency arc with illumination intensity while the low frequency arc is not affected by the illumination, and f) frequency plot illustrates enhancement in the high characteristic frequency. Reproduced with permission.<sup>[57]</sup> Copyright 2020, Royal Society of Chemistry.

inductive loops at low frequencies, were reproduced by DD modeling. Noteworthy, DD simulations have suggested a method for estimating ionic concentration from capacitance-bias voltage measurements.<sup>[140]</sup> Nevertheless, the physical origin of low and high frequency features has still not been fully addressed. The

studies reviewed above have carried out simulations using different measurement protocols including dark measurement at forward biases, different illumination intensities around  $V_{OC}$ , and dark IS analysis at SC. Nevertheless, the impact of some parameters such as temperature, surface recombination velocity, and

ion mobility should be further explored. Furthermore, since the capability of simulating IMPS/IMVS is available in some of the simulators, DD simulation of LIMIS at the same condition as IS may ignite further interest.

#### 4. Light Intensity Modulated Impedance Spectroscopy

Given that solar cells are responsive to optical stimuli, a small AC voltage perturbation during IS measurements can be substituted by small AC light perturbation. This is the foundation for light intensity modulated techniques namely intensity-modulated photovoltage spectroscopy (IMVS), intensity-modulated photocurrent spectroscopy (IMPS), and light intensity modulated impedance spectroscopy (LIMIS). IMPS and IMVS are often considered as complementary techniques to alleviate the complexity of EC modeling in IS with the type of perturbation distinguishing IS from IMPS/IMVS.<sup>[141,142]</sup> A small, sinusoidal voltage perturbs the PSC in IS, whereas a small sinusoidal light perturbation is employed in IMPS/IMVS. IMPS and IMVS experiments are carried out under the same DC conditions (e.g., bias, temperature, illumination, humidity) and the small light perturbation of power density  $\tilde{P}_{in}(t) = |\tilde{P}_{in}| \exp[i\omega t]$  is added to the given DC incident light power density  $\tilde{P}_{in}$ . Although theoretically there is no need for  $\tilde{P}_{in}$ , added DC illumination generally improves signal quality. The electrical response of IMVS and IMPS techniques, is measured in terms of voltage and current to the light perturbation, respectively.<sup>[143]</sup> While IS analyzes transport and recombination processes in the same measurement, IMVS and IMPS have often been used for PSCs to separately characterize recombination and charge transport processes.<sup>[142]</sup> IMPS measures the photocurrent responsivity of PSCs under short circuit condition, whereas for IMVS the photovoltage responsivity of the devices is measured as a function of small light perturbation at zero current, open circuit condition. The Nyquist spectra for IMPS/IMVS show multiple arcs and loops at low frequency part and this region has been the focus of studies to gain useful information about recombination/transport of the PSCs.<sup>[143–145]</sup> In a recent study by Pockett et al., the authors used a combination of IMPS/IMVS measurements with time-domain techniques to explain the behavior of high frequency IMPS/IMVS response.<sup>[143]</sup> They linked the high frequency response to ion migration and interfacial charge recombination at the interface of perovskite with charge selective layers.

IMPS measurements have also been carried out at OC conditions to make it comparable with the results of IS measurements at the same conditions for PSCs.<sup>[141]</sup> An extra feature was observed at intermediate frequencies of IMPS spectra compared to the IS spectra which necessitated the addition of a series  $R-C$  branch to the EC proposed for IMPS.<sup>[146]</sup> By connecting the transfer function of IMPS to external quantum efficiency (EQE) of PSCs, IMPS provided information regarding the recombination and collection efficiency.<sup>[141]</sup>

Some of the main parameters that can be extracted from IMVS/IMPS measurements are recombination lifetimes,<sup>[147–150]</sup> recombination rates, and charge transport properties.<sup>[150–152]</sup> In the following, some studies on IMPS/IMVS are highlighted. Graetzel et al., revealed the effect of Rb doping in triple cation perovskites by means of IMPS and IMVS techniques.<sup>[144]</sup> The

authors observed a reduction in the transport time constant for Rb-doped PSCs of two orders of magnitude compared to control PSCs, indicating the faster extraction of electrons at the layer interface between the Rb-doped perovskite and the charge selective layers. Further, the time response derived from the low frequency feature was correlated to the relaxation of ions. Following this pioneering study, Jo et al., observed a 2.1-fold diffusion coefficient enhancement by IMPS for solvent-engineered perovskite layers in PSCs. *N*-methyl-2-pyrrolidone (NMP) was used as an intercalating solvent to improve the surface morphology of the perovskite absorber layer and the photovoltaic response of the respective PSCs.<sup>[153]</sup> Huang et al., developed CsPbI<sub>3</sub>-based PSCs, by passivating the defects of CsPbI<sub>3</sub> absorber layer with CsBr surface treatments and improving its performance in the presence of light. The Bode plots of IMPS and IMVS measurements revealed the kinetics and mechanism of charge extraction in the dark and under illumination. The CsBr-treated PSC under illumination showed decreased transport time constants from 0.88 to 0.73  $\mu$ s and increased recombination time constants from 4.56 to 5.12  $\mu$ s (compared to the pristine device).<sup>[154]</sup>

LIMIS is a photoimpedance approach which takes advantage of combining data from both IMVS,<sup>[155–159]</sup> and IMPS signals.<sup>[155,156,160–168]</sup> Mathematically, LIMIS is defined as the ratio of IMVS/IMPS and thus described in units of impedance, that is  $\Omega \text{ cm}^2$ . The LIMIS transfer function was first validated via Kramers–Kronig transformation by Song and Macdonald,<sup>[169]</sup> who studied the Nyquist and Bode spectra of n-Si in KOH solution. Subsequently, Halme et al., applied this concept to DSSCs, and presented theoretical deductions of diffusion-based transport equations.<sup>[170,171]</sup> Moreover, when provided with the same steady-state conditions (e.g., DC bias, DC illumination, and temperature), IS and LIMIS provide congruent results. This is stated in Donolato's reciprocity theorem of charge collection:<sup>[172]</sup> the current due to photo-generation at a point surrounded by no charge and the injection of the same charge to the surrounding of the same point are equivalent, if all the remaining boundary conditions are kept identical (e.g. electrostatic potential and illumination at the interfaces toward either the electrodes or the interfaces). Recently, Alvarez et al., proposed an alternative demonstration of the reciprocity theorem via EC theory and showed experimental data suggesting LIMIS  $\cong$  IS obtained from measurements with Si photodiodes.<sup>[173]</sup> In practice, however, the different conditions for the individual measurements of IMPS and IMVS may introduce variations on the boundary conditions and hence the results of IS signal can differ from that of LIMIS.<sup>[114]</sup> As to the transfer function for LIMIS, Almora et al.,<sup>[114]</sup> and Bisquert et al.,<sup>[14,174]</sup> have deduced transport equations for Beer–Lambert and homogeneous generation profiles, respectively. Almora et al., applied the definition of LIMIS to IMPS and IMVS spectra for mixed-cation based PSCs.<sup>[23]</sup>

The schematic characterization of a photovoltaic solar cell at the OC plane is shown in Figure S1, Supporting Information, for IS, IMPS, and IMVS that lead to LIMIS. The LIMIS spectra have been compared to the corresponding IS spectra at OC for different DC illumination intensities shown in **Figure 9a,b**. At low DC illumination intensities, IS presents higher high frequency resistance ( $R_{HF}$ ) than LIMIS, although a series resistance-like effect seemingly affects the LIMIS spectra. At higher frequencies ( $f > 1 \text{ kHz}$ ), the LIMIS spectra results are negative in the Nyquist



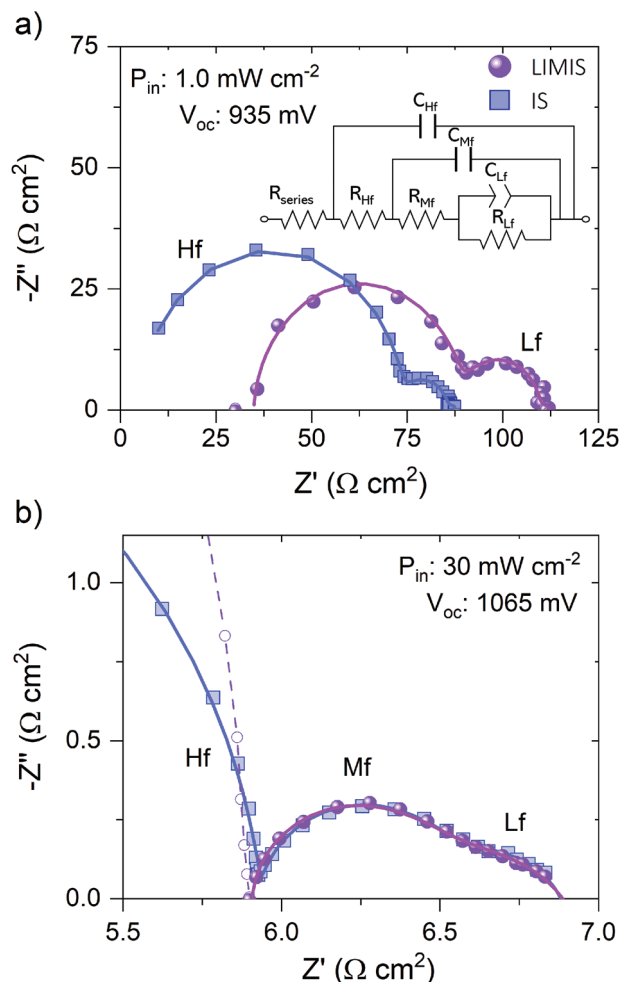


**Figure 9.** LIMIS and IS spectra of a PSC with the structure of ITO/SnO<sub>2</sub>/PMMA(PCBM)/Cs<sub>0.05</sub>MA<sub>0.1</sub>FA<sub>0.85</sub>PbI<sub>2.55</sub>Br<sub>0.45</sub>/PDCBT/Ta-WO<sub>x</sub>/Au at OC under a) lower and b) higher DC illumination intensities, as indicated. Open dots in (b) are the absolute of negative values ( $|-Z''|$ ). Reproduced with permission.<sup>[23]</sup> Copyright 2020, Elsevier.

plot (empty dots in Figure 9b).<sup>[114]</sup> This may suggest the need for further circuit elements to be considered for modeling the high frequency part of the LIMIS spectra and/or the possible occurrence of measurement/calibration artifacts in the HF parts of the IMPS and/or IMVS spectra. The medium and low frequency resistances ( $R_{Mf}$  and  $R_{Lf}$ ) for both IS and LIMIS get closer at high DC illumination intensity (and the corresponding  $V_{OC}$ ). A mismatch was found for some ranges (depending on the sample) of DC illumination, with most discrepancies occurring toward high frequency. The closer IS and LIMIS values approach, the better the charge collection reciprocity theorem is satisfied.<sup>[172]</sup> This may indicate that the charge carrier density profile under high  $P_{in}$  lowers the effective recombination velocity at the interfaces, in comparison to less illuminated conditions.<sup>[114]</sup> The increase of recombination at the interfaces in LIMIS can be associated to the measurement mode of the IMVS which is set to “pure” OC condition. This is fundamentally different than IS and IMPS where the quasi-open-circuit condition is “manually” selected by applying an approximated voltage matching the  $V_{OC}$  which reduces the

DC current enough to be in the range of the AC signal response. By using the IMVS set up, a large resistor prevents any current throughout the sample and thus the recombination velocity is as high as possible for the sample. In addition, the DC charge density profiles and the field distributions should be similar when measuring IS and IMVS, but slightly different in the IMVS experiment. Moreover, these assumptions have been tested for the model of the abrupt-one-sided homojunction solar cell resulting in analytical expressions for the difference between LIMIS and IS proportional to the recombination velocity.<sup>[114]</sup> Even though PSCs are heterojunction solar cells with more complex architecture, it is sensible to suggest that similar mechanisms would take place and therefore, the comparison between IS and LIMIS may be used to detect recombination issues toward the interfaces.

In summary, IS analysis can be complemented with measurements of IMPS and IMVS at the same steady state condition (i.e., DC bias, light, temperature) where the perturbation is optical, instead of electrical. From IMPS and IMVS data it is possible to obtain LIMIS data, whose difference with respect to IS (same units to IS) can be understood in terms of the interface recombination velocities. Nevertheless, there is still a myriad of unknown factors that must be explored. For example, a numerical analysis on what parameters affect the spectral differences between LIMIS and IS in PSCs is still pending. Beyond, further studies could explore dedicated experiments where IS and LIMIS are deliberately driven to diverge, for example by using high energy photon perturbation whose absorption penetration depth would not exceed those of the absorber thickness and the charge carrier diffusion lengths. These experiments may result in different LIMIS spectra upon illumination on an electrode with respect to the other, while IS may not differentiate such situations.

## 5. Applications: IS Studies Based on the Measurement Protocols for PSCs

The most common optimization strategies in multi-layered optoelectronic devices such as PSCs is to attempt to modify: i) the bulk material properties of at least one layer and/or ii) the interface(s) between two consecutive layers, for example, the charge transport layers and the perovskite absorber. These modifications may result in a change in device performance, and a consequent variation in the corresponding IS spectra and characteristic electronic time constants. Therefore, IS has been useful for analyzing PSCs of different device architectures, morphologies, materials, and their subsequent optimization approaches.<sup>[175,176]</sup> The following section gives an overview of recent studies elucidating interface and bulk properties of PSCs by means of IS. Investigating the effect of perovskite crystallinity, Afroz et al., conducted a focus review on monocrystalline PSCs by means of IS. The impedance response of single-crystalline PSCs illustrated a loop at low frequencies which was suggested to be due to vacancy-assisted ionic diffusion in perovskite crystals. The other observed phenomenon by IS was the local changes of carrier density and as a result, electronic conductivity in MAPbBr<sub>3</sub> single crystals which is caused by moving ions.<sup>[177]</sup>

By measuring IS under illumination, Prochowicz et al., analyzed efficient PSCs to find out the origin of low frequency response and its dependence on the parameters such as interface, grain size, and perovskite composition.<sup>[56]</sup> The authors noticed

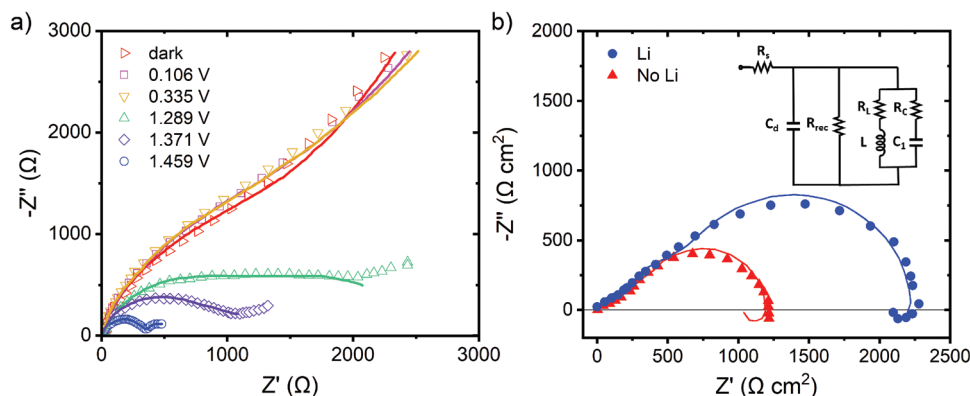


**Figure 10.** a) Impedance spectroscopy of MAPbBr<sub>3</sub> treated by Li<sup>+</sup> at both electron transport layer (ETL) and hole transport layer (HTL) interfaces measured at  $V_{OC}$  under different illumination intensities over a frequency range of 20 mHz to 1 MHz. Reproduced with permission.<sup>[179]</sup> Copyright 2019, American Chemical Society. b) Nyquist plots of pristine and Li<sup>+</sup>-treated MAPbBr<sub>3</sub> at ETL/perovskite interface measured using dark measurement protocol at a voltage bias of 1.1 V. The equivalent circuit (EC) used for the fitting is shown in the inset. Reproduced with permission.<sup>[184]</sup> Copyright 2020, American Chemical Society.

that the  $R_{tr}$  is related to the recombination process and not to the ionic transport. Furthermore, the size of grains was reported to impact the low frequency response the most among the parameters mentioned earlier. In PSCs, the dominant recombination mechanism (bulk or interface) which affects  $V_{OC}$  the most, is still debated. Some strategies to overcome non-radiative recombination and  $V_{OC}$  losses include trap passivation at the perovskite surface and GBs or inserting a thin passivation layer at the interface of perovskite and charge transport layers. Accordingly, the introduction of a thin buffer layer at the interface of perovskite/ETL,<sup>[178–179]</sup> perovskite/HTL,<sup>[180–181]</sup> or at both of the interfaces with the perovskite layer can suppress trap-assisted non-radiative recombination and improve  $V_{OC}$ . Zouhair et al., used a 2D perovskite electron blocking layer at the interface of a 3D perovskite layer and carbon contact.<sup>[182]</sup> IS measurement, under illumination at a negative applied bias of  $-0.6$  V resulted in lower non-radiative recombination and alleviated ion accumulation at this interface according to the high and low frequency resistances in the reported Nyquist plot, respectively. With regards to perovskite/ETL passivation, Yuan et al., were able to reduce interfacial recombination by inserting a thin layer of lithium fluoride (LiF) at the interface of MAPbI<sub>3-x</sub>Cl<sub>x</sub>/SnO<sub>2</sub>.<sup>[178]</sup> IS was performed under illumination for different thicknesses of the LiF layer. By increasing the thickness of the LiF passivation layer, a trade-off between lower trap density (determined from IS) and higher series resistance was found. In a study by Xiong et al., an ionic liquid, tetrabutylammonium hexafluorophosphate (TBAPF<sub>6</sub>), was utilized at the perovskite/PCBM interface as it is an effective passivating agent for perovskites.<sup>[183]</sup> IS results measured under dark condition showed enhanced recombination resistance  $R_{rec}$  at the interface and reduced series resistance  $R_s$  in the presence of the passivator TBAPF<sub>6</sub>.

As for perovskite/HTL interface passivation, Liu et al., used different ammonium salts to make low dimensional perovskite passivation layers at the interface of Cs<sub>0.05</sub>FA<sub>0.95</sub>PbI<sub>2.7</sub>Br<sub>0.3</sub> and Spiro-OMeTAD.<sup>[181]</sup> The IS carried out in the dark at a negative bias of  $-0.9$  V, indicated lower high frequency resistance related to  $R_{tr}$  and large low frequency resistance correlated to  $R_{rec}$  for the modified devices. Therefore, adding a passivation layer re-

sulted in higher charge transfer and lower recombination rates. Similarly, Liang et al., used ammonium salts for passivating the surface of the perovskite films.<sup>[180]</sup> The method using the organic ammonium salt 1-naphthylmethylamine iodide (NMAI) resulted in a large decrease in the non-radiative recombination rate and increase in carrier lifetime and  $V_{OC}$  as indicated by IS measurements. IS measured at a bias of 0.75 V under 1 sun illumination displayed two  $R$ - $C$  constants at low and high frequency regions. The  $R_{tr}$  is much smaller than  $R_{rec}$  and thus, the  $R_{rec}$  can be considered equal to the sum of the low and high frequency resistances.

For the passivation of both HTL and ETL interfaces in the goal of reducing undesired recombination mechanisms and improving open-circuit voltage, Aranda et al., performed a lithium treatment at both interfaces of mesoporous TiO<sub>2</sub> and Spiro-OMeTAD layers with wide-bandgap MAPbBr<sub>3</sub> PSCs.<sup>[179]</sup> The impedance responses were measured at  $V_{OC}$  under different illumination intensities and showed larger high frequency  $R_{rec}$  for the PSCs when both charge transporting layers were treated with Li<sup>+</sup> ions compared to the pristine device. Figure 10a shows two arcs in the IS plots related to the recombination of carriers. Decrease in  $R_{rec}$  was associated with an enhancement in photovoltage of the treated PSC. In this respect, in another study, negative capacitance behavior in the low frequency region of Li<sup>+</sup>-treated MAPbBr<sub>3</sub> cells was analyzed using SPM.<sup>[184]</sup> The negative capacitance feature in the impedance response which was measured using dark measurement protocol at the bias of 1.1 V, was modeled using an inductance in the  $R_L$ - $L$  branch of an EC. Samples with smaller negative capacitance (Li<sup>+</sup> treatment at ETL/perovskite) showed much higher recombination resistance than the pristine samples due to lower density of holes accumulated at the ETL/perovskite interface (Figure 10b).

Similarly, a 2D perovskite interlayer was employed by Almora et al., at the interface of 3D perovskite materials, MAPbI<sub>3</sub> and Cs<sub>0.1</sub>FA<sub>0.74</sub>MA<sub>0.13</sub>PbI<sub>2.48</sub>Br<sub>0.39</sub> (CFMPiB), and their neighboring charge transport layers in three different structures of 3D/2D/ETL, HTL/2D/3D, and 2D/3D/2D.<sup>[185]</sup>

Figure 11a–d illustrates the IS response of MAPbI<sub>3</sub> and CFMPiB perovskites measured under different light intensities at OC condition which is believed to be a suitable condition for

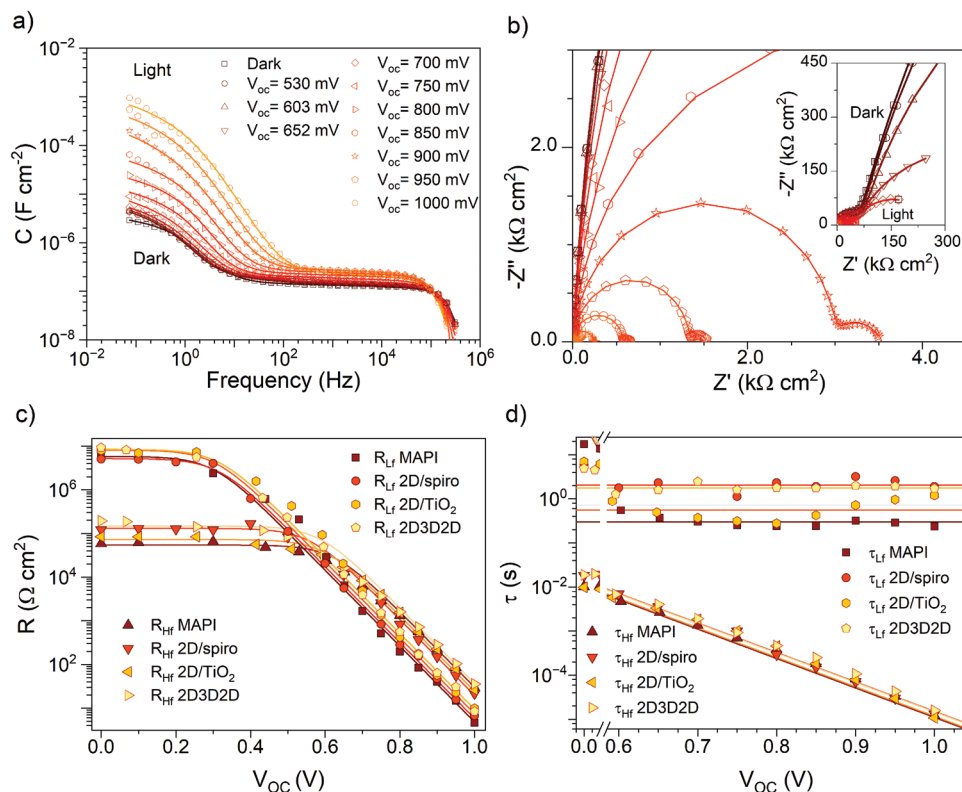


**Figure 11.** Impedance response of MAPbI<sub>3</sub> solar cells measured under illumination at OC including: a) Capacitance–frequency and b) Nyquist plots representing two features at high and low frequencies, c) recombination resistance,  $R$ , and d) characteristic response time,  $\tau$  calculated for four structures of: 3D MAPbI<sub>3</sub>, 2D/Spiro-OMeTAD, 2D/TiO<sub>2</sub>, and 2D/3D/2D. The low and high frequency recombination resistances are reported to be associated with surface and bulk recombination, respectively. Reproduced with permission.<sup>[185]</sup> Copyright 2021, Academics.

identifying bulk and interface features. In Figure 11a,  $C_{Lf}$  gradually rises with illumination intensity/voltage and is influenced by a slow relaxation time constant which is related to the ionic kinetics.  $C_{Hf}$ , on the other hand, was reported to be approximately constant with illumination intensity/voltage and is interpreted as the geometrical capacitance  $C_g$ . The IS response in Figure 11b displays two features at low and high frequencies. The response at low frequency is associated with ion motion and surface recombination, which is suggested to be the dominant reason behind  $J$ – $V$  hysteresis; whereas the high frequency feature has been correlated with bulk recombination.<sup>[186]</sup> Regarding the resistances, Figure 11c shows that  $R_{Lf}$  which most likely relates to the surface recombination mechanism, is much higher than  $R_{Hf}$  under low illumination intensity/voltage. In contrast, a higher  $R_{Hf}$  than  $R_{Lf}$  at higher illumination intensity/voltage was related to a higher injection current and bulk radiative recombination, and consequently a higher significance of bulk phenomena at high illumination intensities/voltages. The almost constant low frequency characteristic time  $\tau_{Lf} = R_{Lf} C_{Lf}$  with bias (Figure 11d) was explained with inverse changes of resistance with photocurrent since more charge is stored in the capacitance with photocurrent flow.<sup>[29]</sup>  $\tau_{Lf}$  is reported to be a sign of ionic phenomena occurring at the interfaces. The high frequency characteristic response time  $\tau_{Hf}$ , on the contrary, continued to decrease with illumination intensity/voltage as shown in Figure 11d. This is due to the faster recombination of photo-charges stored in the

charge transport layers with interface defects under high illumination intensity.<sup>[187]</sup> Nevertheless, in this study, the inclusion of a 2D interlayer in mixed-cation devices did not lead to a significant change in the bulk recombination rate and thus in the value of  $V_{OC}$ .<sup>[29]</sup>

In summary, this section highlighted the application of IS measurement protocols in elucidating the carrier dynamics of PSCs. Several research works were discussed that mostly studied surface treatment at the interfaces of perovskite with its adjacent layers. In most of the cases, lower recombination rate and better carrier extraction were obtained which resulted in higher performance due to interface modifications.

## 6. Discussion

In this review, the commonly used IS measurement protocols for analyzing PSCs were explained. A myriad of theories are suggested to interpret IS results in PSCs making it challenging to understand and assign the origin of some features, most notably the low frequency response. Despite good consensus of the understanding of high frequency response, the physical nature of low frequency impedance response is still mostly ambiguous and poses challenges in defining a general circuit for this part of the impedance spectrum.<sup>[36]</sup>

### 6.1. Measurement Conditions and Device Stability

The selected measurement conditions for IS are of paramount importance for the extracted parameters and learnings from the data obtained. IS measurements can be conducted at different operating points (e.g.,  $V_{OC}$ ,  $J_{SC}$ , and MPP) of the  $J$ - $V$  curve. However,<sup>[36]</sup> IS analysis at  $V_{OC}$  may be considered the most useful and informative measurement for PSCs due to its well-defined nature of the operating point and the linearity condition for IS measurement being satisfied at this point. An important protocol for IS measurement at  $V_{OC}$  is ORIS which is explained in Section 2.2. Besides performing IS measurement at  $V_{OC}$ , other factors for attaining the linearity conditions are important. An example for this is the adequate selection of the value for the AC perturbation voltage, where the latter should be low enough (typically  $\approx 10$ – $20$  mV) to satisfy linearity conditions, but high enough to reduce noise in the impedance signal. To dwindle the impact of unwanted stimuli on IS response and maintain the stability of PSC devices during IS measurement, it is advisable to use a Faraday cage and shield the cables and connectors both in dark and under light conditions. To reduce the influence of RH and cell degradation during experiments, dry air purge system can be connected to the Faraday cage or PSCs can be encapsulated. IS measurements under light may accelerate device degradation; however, it is closer to the real operating condition of the device and should thus receive more attention. Pre-conditioning the samples, for example pre-biasing in M–S measurement to voltages above the  $V_{OC}$  values, may further deteriorate the device. In this case, it is good practice to specify the upper current limit of the potentiostat. To understand and monitor the influence of the PSCs degradation during characterization,  $J$ - $V$  measurements immediately before and after IS analysis should be carried out. In this regard, we would like to invite researchers to report the pre- and post-measurement PCEs of the devices under test (DUT) to foster the development of reproducible IS measurement practices and fundamental device understanding in the field.<sup>[188]</sup>

### 6.2. Equivalent Circuit Modeling

It is worth to stress the importance of the three principles for EC modeling: 1) Accuracy of modeling, which can be verified by the fitting error which is available in most software for data analysis. Ideally, fitted data should be depicted alongside the data; 2) Physical representiveness of the EC. This principle should also consider the measurement condition in which the impedance response was obtained. For example, at SC condition with significant current flow, more inductive behaviors may be expected; 3) Principle of generality, which means that the designed EC should describe the IS response at different measurement conditions, for example in dark at forward biases or ORIS. Therefore, all the parameters that define the device condition such as frequency, DC bias, and illumination intensity should follow the generality rule for EC modeling. Furthermore, there is a trade-off between physical understanding of an EC and its complexity. Simple ECs may be easy to interpret but may not fully capture the data and explain the carrier dynamics of PSCs. Conversely, for complex ECs that may accurately reproduce data may prove challenging to correlate each circuit element with physical phenomena in the

device. Further it is good practice to follow the rule of “more than one spectrum per sample.” To elucidate performance improvements in PSCs, it is common to compare the impedance response of a treated device with its reference counterpart. To increase confidence in the assessment, however, it is suggested to measure more than one spectrum per device.

### 6.3. Characterization Methods

For M–S analysis, pre-biasing is performed to remove the effect of other capacitances on the depletion capacitance. Although, it is a good guideline for M–S analysis, the question remains whether this effect reveals the underlying immobile doping density and built-in field, or if it merely reflects the capability of the mobile ions to modify the charge density profile. For IS characterization under light, ORIS is a convenient choice due to the low inductive effects and minimal instability (unlike SC and MPP), the high linearity of the AC signal (unlike MPP), and a practical energy diagram where the flat bands/quasi-Fermi levels are in agreement with several theoretical models and thus eases the quantification of  $R_{rec}$  and  $C_{\mu}$ .<sup>[189]</sup>

### 6.4. Complementary Methods for IS Analysis

The motivation for the recent research studies on numerical simulation of impedance responses is mainly due to the advantages of these methods in interpreting the impedance responses. In some cases, the obtained IS spectra are too complex or distorted to fit using the common EC models for PSCs. Therefore, it is not always possible to understand all the physical phenomena via fitting with the EC models. This challenge is currently fueling the interest in numerical modeling of impedance spectra using methods reviewed in this article, that is, DD modeling and light-intensity modulated methods. Notably, several ECs have been reported that can describe IS data only inadequately or incompletely, prompting the need for further EC elements which would complicate understanding further. Here, progressing supportive numerical methods may be able to aid in interpreting the physical meaning of collected impedance data.

## 7. Conclusions

Impedance spectroscopy is an important, non-destructive tool for the electrical characterization of PSCs with a myriad of available compositions, device architectures, fabrication methods, morphologies, and performance (both improvements and degradation). The most common measurement protocols including dark measurements at different DC biases, capacitance spectroscopy, M–S, TAS, ORIS, and ECIS were discussed in this review. For the TAS protocol, we showed the minimum trap density measurable via capacitive techniques and the maximum trap density which is limited by the effective density of states at the band edges. Most of the reviewed studies had their trap densities between these two limits with only a few of them close to or above the upper limit. PSCs were also analyzed in terms of activation energy and PCE. Another analysis was done in ORIS section to confirm the constant and declining trend of low and high frequency characteristic

response times as a function of  $V_{OC}$  for different PSCs, respectively. Furthermore, this review highlighted the recent advances in DD modeling of impedance responses, and summarized the most common DD-based simulators in PSCs. As a complementary method, LIMIS showed comparable results to IS, although further investigation is needed in the high frequency part of the LIMIS spectra. A section reviewing the applications of IS measurement protocols in PSCs were also added to mainly show the influence of interface engineering on the performance of these devices. With growing efforts in perovskite research towards the technology's PCE limits, further phenomenological understanding via IS will be critical to understand limitations and overcome hurdles on its path towards commercialization.

## Supporting Information

Supporting Information is available from the Wiley Online Library or from the author.

## Acknowledgements

The authors acknowledge that this work was conducted on the traditional, ancestral, and unceded territory of the Syilx Okanagan Nation (Kelowna). E.G., S.S., A.A.D., T.H.C., and A.R.U. acknowledge the financial support provided by the Natural Sciences and Engineering Research Council of Canada (NSERC) through grants RGPIN-2019-05489 and DGEER-2019-00450 as well as the Canada Foundation for Innovation (CFI) and British Columbia Knowledge Development Fund (BCKDF) through grant 39081. O.A. thanks the Spanish State Research Agency (Agencia Estatal de Investigación) for the Juan de la Cierva 2021 postdoctoral fellowship. Discussions with Prof. Germà Garcia-Belmonte (Institute of Advanced Materials (INAM), Spain) are acknowledged.

## Conflict of Interest

The authors declare no conflict of interest.

## Keywords

characterization protocols, drift-diffusion numerical simulation, impedance spectroscopy, light-intensity modulated impedance spectroscopy, perovskite solar cells

Received: December 24, 2022

Revised: May 20, 2023

Published online: July 3, 2023

- [1] J. B. Mascarell, E. J. J. Pérez, P. V. Kamat, *Hybrid Perovskite Solar Cells: The Genesis and Early Developments, 2009–2014*, Fundació Scito, Valencia, Spain 2017. /bib>
- [2] J. Park, J. Kim, H.-S. Yun, M. J. Paik, E. Noh, H. J. Mun, M. G. Kim, T. J. Shin, S. I. Seok, *Nature* **2023**, 724.
- [3] M. A. Green, E. Dunlop, G. Siefert, M. Yoshita, N. Kopidakis, K. Bothe, X. Hao, *Prog. Photovoltaics* **2023**, 31, 3.
- [4] O. Almora, D. Baran, G. C. Bazan, C. I. Cabrera, S. Erten-Ela, K. Forberich, F. Guo, J. Hauch, A. W. Y. Ho-Baillie, T. J. Jacobsson, R. A. J. Janssen, T. Kirchartz, N. Kopidakis, M. A. Loi, R. R. Lunt, X.

- Mathew, M. D. McGehee, J. Min, D. B. Mitzi, M. K. Nazeeruddin, J. Nelson, A. F. Nogueira, U. W. Paetzold, B. P. Rand, U. Rau, H. J. Snaith, E. Unger, L. Vaillant-Roca, C. Yang, H.-L. Yip, *Adv. Energy Mater.* **2022**, 13, 2203313.
- [5] B. Abdollahi Nejand, I. M. Hossain, M. Jakoby, S. Moghadamzadeh, T. Abzieher, S. Gharibzadeh, J. A. Schwenzer, P. Nazari, F. Schackmar, D. Hauschild, *Adv. Energy Mater.* **2020**, 10, 1902583.
- [6] P. S. Schulze, A. J. Bett, M. Bivour, P. Caprioglio, F. M. Gerspacher, Ö. Ş. Kabaklı, A. Richter, M. Stolterfoht, Q. Zhang, D. Neher, *Sol. RRL* **2020**, 4, 2000152.
- [7] D. Di Girolamo, N. Phung, F. U. Kosasih, F. Di Giacomo, F. Matteocci, J. A. Smith, M. A. Flatken, H. Köbler, S. H. Turren Cruz, A. Mattoni, *Adv. Energy Mater.* **2020**, 10, 2000310.
- [8] O. Almora, P. Lopez-Varo, K. T. Cho, S. Aghazada, W. Meng, Y. Hou, C. Echeverría-Arrondo, I. Zimmermann, G. J. Matt, J. A. Jiménez-Tejada, *Sol. Energy Mater. Sol. Cells* **2019**, 195, 291.
- [9] P. Lopez-Varo, J. A. Jiménez-Tejada, M. García-Rosell, S. Ravishanker, G. Garcia-Belmonte, J. Bisquert, O. Almora, *Adv. Energy Mater.* **2018**, 8, 1702772.
- [10] S. Ravishanker, O. Almora, C. Echeverría-Arrondo, E. Ghahremanirad, C. Aranda, A. Guerrero, F. Fabregat-Santiago, A. Zaban, G. Garcia-Belmonte, J. Bisquert, *J. Phys. Chem. Lett.* **2017**, 8, 915.
- [11] E. L. Unger, E. T. Hoke, C. D. Bailie, W. H. Nguyen, A. R. Bowring, T. Heumüller, M. G. Christoforo, M. D. McGehee, *Energy Environ. Sci.* **2014**, 7, 3690.
- [12] H. J. Snaith, A. Abate, J. M. Ball, G. E. Eperon, T. Leijtens, N. K. Noel, S. D. Stranks, J. T.-W. Wang, K. Wojciechowski, W. Zhang, *J. Phys. Chem. Lett.* **2014**, 5, 1511.
- [13] J. Jiménez-López, E. Palomares, *Nanoscale* **2019**, 11, 20024.
- [14] J. Bisquert, M. Janssen, *J. Phys. Chem. Lett.* **2021**, 12, 7964.
- [15] W. Wang, D. Zhang, R. Liu, D. T. Gangadharan, F. Tan, M. I. Saidaminov, *J. Semicond.* **2022**, 43, 051202.
- [16] W. S. Yang, B.-W. Park, E. H. Jung, N. J. Jeon, Y. C. Kim, D. U. Lee, S. S. Shin, J. Seo, E. K. Kim, J. H. Noh, *Science* **2017**, 356, 1376.
- [17] L. Bertoluzzi, P. P. Boix, I. Mora-Sero, J. Bisquert, *J. Phys. Chem. C* **2014**, 118, 16574.
- [18] J. Bisquert, L. Bertoluzzi, I. Mora-Sero, G. Garcia-Belmonte, *J. Phys. Chem. C* **2014**, 118, 18983.
- [19] G. R. Neupane, M. Bamidele, V. Yeddu, D. Y. Kim, P. Hari, *J. Mater. Res.* **2022**, 37, 1357.
- [20] F. Ebadi, N. Taghavinia, R. Mohammadpour, A. Hagfeldt, W. Tress, *Nat. Commun.* **2019**, 10, 1574.
- [21] E. Ghahremanirad, A. Bou, S. Olyaei, J. Bisquert, *J. Phys. Chem. Lett.* **2017**, 8, 1402.
- [22] V. K. Sangwan, M. Zhu, S. Clark, K. A. Luck, T. J. Marks, M. G. Kanatzidis, M. C. Hersam, *ACS Appl Mater Interfaces* **2019**, 11, 14166.
- [23] O. Almora, Y. Zhao, X. Du, T. Heumueller, G. J. Matt, G. Garcia-Belmonte, C. J. Brabec, *Nano Energy* **2020**, 75, 104982.
- [24] K. Gesi, *Ferroelectrics* **1997**, 203, 249.
- [25] O. Almora, G. Garcia-Belmonte, *Sol. Energy* **2019**, 189, 103.
- [26] O. Almora, C. Aranda, E. Mas-Marzá, G. Garcia-Belmonte, *Appl. Phys. Lett.* **2016**, 109, 173903.
- [27] M. Fischer, K. Tvingstedt, A. Baumann, V. Dyakonov, *ACS Appl. Energy Mater.* **2018**, 1, 5129.
- [28] O. Almora, M. García-Batlle, G. Garcia-Belmonte, *J. Phys. Chem. Lett.* **2019**, 10, 3661.
- [29] O. Almora, K. T. Cho, S. Aghazada, I. Zimmermann, G. J. Matt, C. J. Brabec, M. K. Nazeeruddin, G. Garcia-Belmonte, *Nano Energy* **2018**, 48, 63.
- [30] O. Almora, A. González-Lezcano, A. Guerrero, C. J. Brabec, G. Garcia-Belmonte, *J. Appl. Phys.* **2020**, 128, 075104.

- [31] O. Almora, I. Zarazua, E. Mas-Marza, I. Mora-Sero, J. Bisquert, G. Garcia-Belmonte, *J. Phys. Chem. Lett.* **2015**, *6*, 1645.
- [32] D. Pitarch-Tena, T. T. Ngo, M. Vallés-Pelarda, T. Pauporté, I. Mora-Seró, *ACS Energy Lett.* **2018**, *3*, 1044.
- [33] G. Murugadoss, S. Tanaka, G. Mizuta, S. Kanaya, H. Nishino, T. Umeyama, H. Imahori, S. Ito, *Jpn. J. Appl. Phys.* **2015**, *54*, 08KF08.
- [34] W. Chi, S. K. Banerjee, *Chem. Mater.* **2021**, *33*, 4269.
- [35] J. Li, R. Xia, W. Qi, X. Zhou, J. Cheng, Y. Chen, G. Hou, Y. Ding, Y. Li, Y. Zhao, X. Zhang, *J. Power Sources* **2021**, *485*, 229313.
- [36] E. von Hauff, D. Klotz, *J. Mater. Chem. C* **2022**, *10*, 742.
- [37] P. Yadav, M. I. Dar, N. Arora, E. A. Alharbi, F. Giordano, S. M. Zakeeruddin, M. Grätzel, *Adv. Mater.* **2017**, *29*, 1701077.
- [38] Q. Dong, Y. Fang, Y. Shao, P. Mulligan, J. Qiu, L. Cao, J. Huang, *Science* **2015**, *347*, 967.
- [39] Y. Feng, J. Bian, Q. Dong, H. Ma, W. Zhao, S. Wang, J. Liu, R. Chen, Y. Shi, *ACS Appl. Energy Mater.* **2020**, *3*, 8017.
- [40] A. Guerrero, J. Bisquert, G. Garcia-Belmonte, *Chem. Rev.* **2021**, *121*, 14430.
- [41] S.-M. Yoo, S. J. Yoon, J. A. Anta, H. J. Lee, P. P. Boix, I. Mora-Seró, *Joule* **2019**, *3*, 2535.
- [42] C. Gonzales, A. Guerrero, J. Bisquert, *J. Phys. Chem. C* **2022**, *126*, 13560.
- [43] R. Yekani, H.-c. Chiu, D. Strandell, Z. Wang, S. Bessette, R. Gauvin, P. Kambhampati, G. P. Demopoulos, *Nanoscale* **2023**, *15*, 2152.
- [44] S. Sandhu, C. Saharan, S. K. Buruga, S. A. Kumar, P. S. Rana, P. Nagajyothi, S. D. Mane, *Ceram. Int.* **2021**, *47*, 14665.
- [45] J.-F. Liao, W.-Q. Wu, J.-X. Zhong, Y. Jiang, L. Wang, D.-B. Kuang, *J. Mater. Chem. A* **2019**, *7*, 9025.
- [46] F. Yang, M. A. Kamarudin, G. Kapil, D. Hirotani, P. Zhang, C. H. Ng, T. Ma, S. Hayase, *ACS Appl. Mater. Interfaces* **2018**, *10*, 24543.
- [47] S. Wozny, M. Yang, A. M. Nardes, C. C. Mercado, S. Ferrere, M. O. Reese, W. Zhou, K. Zhu, *Chem. Mater.* **2015**, *27*, 4814.
- [48] D. R. Ceratti, A. Zohar, R. Kozlov, H. Dong, G. Uraltsev, O. Girshevitz, I. Pinkas, L. Avram, G. Hodes, D. Cahen, *Adv. Mater.* **2020**, *32*, 2002467.
- [49] J. H. Noh, S. H. Im, J. H. Heo, T. N. Mandal, S. I. Seok, *Nano Lett.* **2013**, *13*, 1764.
- [50] E. Jocar, P. H. Hou, S. S. Bhosale, H. S. Chuang, S. Narra, E. Wei-Guang Diau, *ChemSusChem* **2021**, *14*, 4415.
- [51] D. Song, S. Narra, M.-Y. Li, J.-S. Lin, E. W.-G. Diau, *ACS Energy Lett.* **2021**, *6*, 4179.
- [52] Y. Wang, T. Li, X. Chen, L. Zhang, *Mater. Lett.* **2022**, *321*, 132460.
- [53] S. Ravishankar, Z. Liu, U. Rau, T. Kirchartz, *PRX Energy* **2022**, *1*, 013003.
- [54] M. Taukeer Khan, F. Khan, A. Al-Ahmed, S. Ahmad, F. Al-Sulaiman, *Chem. Rec.* **2022**, *22*, e202100330.
- [55] R. A. Awni, Z. Song, C. Chen, C. Li, C. Wang, M. A. Razooqi, L. Chen, X. Wang, R. J. Ellingson, J. V. Li, Y. Yan, *Joule* **2020**, *4*, 644.
- [56] D. Prochowicz, S. Trivedi, N. Parikh, M. Saliba, A. Kalam, M. M. Tavakoli, P. Yadav, *Energy Technol.* **2021**, *9*, 2100229.
- [57] A. Riquelme, L. J. Bennett, N. E. Courtier, M. J. Wolf, L. Contreras-Bernal, A. B. Walker, G. Richardson, J. A. Anta, *Nanoscale* **2020**, *12*, 17385.
- [58] I. M. Dharmadasa, Y. Rahaq, A. A. Ojo, T. I. Alanazi, *J. Mater. Sci.: Mater. Electron.* **2019**, *30*, 1227.
- [59] A. Urbaniak, A. Czudek, J. Dagar, E. L. Unger, *Sol. Energy Mater. Sol. Cells* **2022**, *238*, 111618.
- [60] L. McGovern, I. Koschany, G. Grimaldi, L. A. Muscarella, B. Ehrler, *J. Phys. Chem. Lett.* **2021**, *12*, 2423.
- [61] W. A. Laban, L. Etgar, *Energy Environ. Sci.* **2013**, *6*, 3249.
- [62] S. M. Willis, C. Cheng, H. E. Assender, A. A. Watt, arXiv:1112.1623, **2011**.
- [63] C. van Opdorp, *Solid-State Electron.* **1968**, *11*, 397.
- [64] S. M. Sze, K. K. Ng, *Physics of Semiconductor Devices*, John Wiley & Sons, Hoboken, NJ **2007**, p. 832.
- [65] H. Kleemann, B. Lüssem, K. Leo, *J. Appl. Phys.* **2012**, *111*, 123722.
- [66] M. H. Kumar, S. Dharani, W. L. Leong, P. P. Boix, R. R. Prabhakar, T. Baikie, C. Shi, H. Ding, R. Ramesh, M. Asta, M. Graetzel, S. G. Mhaisalkar, N. Mathews, *Adv. Mater.* **2014**, *26*, 7122.
- [67] H. Ban, Z. Zhang, L. Dai, Z. Liu, H. Yu, Y. Shen, X.-L. Zhang, J. Zhu, M. Wang, *Sol. RRL* **2022**, *6*, 2200827.
- [68] K. Zhang, A. Späth, O. Almora, V. M. Le Corre, J. Wortmann, J. Zhang, Z. Xie, A. Barabash, M. S. Hammer, T. Heumüller, J. Min, R. Fink, L. Lüer, N. Li, C. J. Brabec, *ACS Energy Lett.* **2022**, *7*, 3235.
- [69] B.-X. Chen, H.-S. Rao, W.-G. Li, Y.-F. Xu, H.-Y. Chen, D.-B. Kuang, C.-Y. Su, *J. Mater. Chem. A* **2016**, *4*, 5647.
- [70] L. Xie, J. Wang, K. Liao, J.-a. Yang, A. Wang, X. Deng, C. Li, T. Li, X. Niu, F. Hao, *J. Mater. Chem. A* **2019**, *7*, 18626.
- [71] F. Peña-Camargo, J. Thiesbrummel, H. Hempel, A. Musiienko, V. M. L. Corre, J. Diekmann, J. Warby, T. Unold, F. Lang, D. Neher, arXiv:2201.09664, **2022**.
- [72] D. B. Khadka, Y. Shirai, M. Yanagida, K. Miyano, *J. Mater. Chem. C* **2020**, *8*, 2307.
- [73] S. J. Lee, S. S. Shin, J. Im, T. K. Ahn, J. H. Noh, N. J. Jeon, S. I. Seok, J. Seo, *ACS Energy Lett.* **2018**, *3*, 46.
- [74] S. Shao, J. Liu, G. Portale, H.-H. Fang, G. R. Blake, G. H. ten Brink, L. J. A. Koster, M. A. Loi, *Adv. Energy Mater.* **2018**, *8*, 1702019.
- [75] C. Wang, F. Gu, Z. Zhao, H. Rao, Y. Qiu, Z. Cai, G. Zhan, X. Li, B. Sun, X. Yu, B. Zhao, Z. Liu, Z. Bian, C. Huang, *Adv. Mater.* **2020**, *32*, 1907623.
- [76] C. Quarti, E. Mosconi, J. M. Ball, V. D'Innocenzo, C. Tao, S. Pathak, H. J. Snaith, A. Petrozza, F. De Angelis, *Energy Environ. Sci.* **2016**, *9*, 155.
- [77] Q. Dong, C. H. Y. Ho, H. Yu, A. Salehi, F. So, *Chem. Mater.* **2019**, *31*, 6833.
- [78] B. Chen, H. Hu, T. Salim, Y. M. Lam, *J. Mater. Chem. C* **2019**, *7*, 5646.
- [79] H. Yu, M. Wang, C. Han, K. Wang, B. Hu, *Nano Energy* **2020**, *67*, 104285.
- [80] S. H. Cho, J. Byeon, K. Jeong, J. Hwang, H. Lee, J. Jang, J. Lee, T. Kim, K. Kim, M. Choi, *Adv. Energy Mater.* **2021**, *11*, 2100555.
- [81] L. Bai, F. Yao, R. Wang, B. Liu, D. He, Q. Zhou, W. Wang, C. Xu, X. Hu, S. Chen, Q. Song, T. Zhou, D. Lee, P. Zhao, C. Chen, H. Yang, Q. Lin, Z. Zang, J. Chen, *Sci. China Mater.* **2022**, *65*, 3368.
- [82] S. Tang, Y. Peng, Z. Zhu, J. Zong, L. Zhao, L. Yu, R. Chen, M. Li, *J. Phys. Chem. Lett.* **2022**, *13*, 5116.
- [83] W.-Q. Wu, Z. Yang, P. N. Rudd, Y. Shao, X. Dai, H. Wei, J. Zhao, Y. Fang, Q. Wang, Y. Liu, *Sci. Adv.* **2019**, *5*, eaav8925.
- [84] M. Li, Z. K. Wang, M. P. Zhuo, Y. Hu, K. H. Hu, Q. Q. Ye, S. M. Jain, Y. G. Yang, X. Y. Gao, L. S. Liao, *Adv. Mater.* **2018**, *30*, 1800258.
- [85] S. Gharibzadeh, P. Fassel, I. M. Hossain, P. Rohrbeck, M. Frericks, M. Schmidt, M. R. Khan, T. Abzieher, B. A. Nejang, F. Schackmar, *Energy Environ. Sci.* **2021**, *14*, 5875.
- [86] S. Ravishankar, T. Unold, T. Kirchartz, *Science* **2021**, *371*, eabd8014.
- [87] J. Bisquert, F. Fabregat-Santiago, I. Mora-Seró, G. Garcia-Belmonte, S. Giménez, *J. Phys. Chem. C* **2009**, *113*, 17278.
- [88] J. Bisquert, *J. Phys. Chem. Lett.* **2022**, *13*, 7320.
- [89] C. Aranda, J. Bisquert, A. Guerrero, *J. Chem. Phys.* **2019**, *151*, 124201.
- [90] T. S. Rapolles, P. Serafini, C. Redondo-Obispo, E. Climent-Pascual, S. Masi, I. Mora-Seró, C. Coya, *Energy Technol.* **2022**, *10*, 2100890.
- [91] A. Castro-Chong, A. J. Riquelme, T. Aernouts, L. J. Bennett, G. Richardson, G. Oskam, J. A. Anta, *ChemPlusChem* **2021**, *86*, 1347.
- [92] L. Contreras-Bernal, S. Ramos-Terrón, A. Riquelme, P. P. Boix, J. Idigoras, I. Mora-Seró, J. A. Anta, *J. Mater. Chem. A* **2019**, *7*, 12191.
- [93] L. J. Bennett, A. J. Riquelme, N. E. Courtier, J. A. Anta, G. Richardson, arXiv:2105.11226, **2021**.
- [94] L. J. Bennett, A. J. Riquelme, J. A. Anta, N. E. Courtier, G. Richardson, *Phys. Rev. Appl.* **2023**, *19*, 014061.

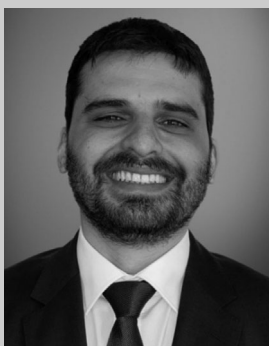
- [95] O. Almora, J. Wiegand, P. López-Varo, G. J. Matt, C. J. Brabec, *Sol. RRL* **2021**, 5, 2100024.
- [96] T. M. Clarke, C. Lungenschmied, J. Peet, N. Drolet, A. J. Mozer, *Adv. Energy Mater.* **2015**, 5, 1401345.
- [97] P. R. Barnes, K. Miettunen, X. Li, A. Y. Anderson, T. Bessho, M. Gratzel, B. C. O'Regan, *Adv. Mater.* **2013**, 25, 1881.
- [98] Z. S. Wang, F. Ebadi, B. Carlsen, W. C. H. Choy, W. Tress, *Small Methods* **2020**, 4, 2000290.
- [99] S. M. Abdulrahim, Z. Ahmad, J. Bhadra, N. J. Al-Thani, *Molecules* **2020**, 25, 5794.
- [100] A. Todinova, L. Contreras-Bernal, M. Salado, S. Ahmad, N. Morillo, J. Idígoras, J. A. Anta, *ChemElectroChem* **2017**, 4, 2891.
- [101] M. R. Shoar Abouzari, F. Berkemeier, G. Schmitz, D. Wilmer, *Solid State Ionics* **2009**, 180, 922.
- [102] Z. Ahmad, A. Mishra, S. M. Abdulrahim, F. Touati, *J. Electroanal. Chem.* **2020**, 871, 114294.
- [103] B. Romero, G. del Pozo, B. Arredondo, D. Martín-Martín, E. Hernández-Balaguera, M. d. C. L. González, *Women Renewable Energy* **2019**, 110950, 110950N.
- [104] O. Almora, L. G. Gerling, C. Voz, R. Alcubilla, J. Puigdollers, G. Garcia-Belmonte, *Sol. Energy Mater. Sol. Cells* **2017**, 168, 221.
- [105] A. R. Pascoe, N. W. Duffy, A. D. Scully, F. Huang, Y.-B. Cheng, *J. Phys. Chem. C* **2015**, 119, 4444.
- [106] C. Ng, H. Lim, S. Hayase, Z. Zainal, N. Huang, *Renewable Sustainable Energy Rev.* **2018**, 90, 248.
- [107] S. Yuan, Y. Cai, S. Yang, H. Zhao, F. Qian, Y. Han, J. Sun, Z. Liu, S. Liu, *Sol. RRL* **2019**, 3, 1900220.
- [108] M. Jeong, I. W. Choi, E. M. Go, Y. Cho, M. Kim, B. Lee, S. Jeong, Y. Jo, H. W. Choi, J. Lee, *Science* **2020**, 369, 1615.
- [109] D. Yang, R. Yang, K. Wang, C. Wu, X. Zhu, J. Feng, X. Ren, G. Fang, S. Priya, S. F. Liu, *Nat. Commun.* **2018**, 9, 3239.
- [110] H. B. Lee, N. Kumar, M. M. Ovhal, Y. J. Kim, Y. M. Song, J. W. Kang, *Adv. Funct. Mater.* **2020**, 30, 2001559.
- [111] D. A. Jacobs, H. Shen, F. Pfeffer, J. Peng, T. P. White, F. J. Beck, K. R. Catchpole, *J. Appl. Phys.* **2018**, 124, 225702.
- [112] D. Moia, I. Gelmetti, P. Calado, W. Fisher, M. Stringer, O. Game, Y. Hu, P. Docampo, D. Lidzey, E. Palomares, *Energy Environ. Sci.* **2019**, 12, 1296.
- [113] M. S. Alvar, P. W. Blom, G.-J. A. Wetzelaer, *Nat. Commun.* **2020**, 11, 4023.
- [114] O. Almora, D. Miravet, G. J. Matt, G. Garcia-Belmonte, C. J. Brabec, *Appl. Phys. Lett.* **2020**, 116, 013901.
- [115] M. Burgelman, P. Nollet, S. Degraeve, *Thin Solid Films* **2000**, 361–362, 527.
- [116] M. Zeman, J. van den Heuvel, M. Kroon, J. Willems, B. Pieters, J. Krc, S. Solntsev in *Advanced Semiconductor Analysis (ASA)*, Delft University of Technology, The Netherlands **2011**. <https://www.tudelft.nl/en/ewi/over-de-faculteit/afdelingen/electrical-sustainable-energy/photovoltaic-materials-and-devices/software-platform/asa-software>.
- [117] M. A. d. Maur, G. Penazzi, G. Romano, F. Sacconi, A. Pecchia, A. D. Carlo, *IEEE Trans. Electron Devices* **2011**, 58, 1425.
- [118] S. Michael, P. Michalopoulos, in *2002 45th Midwest Symp. on Circuits and Systems, MWSCAS-2002, IEEE, Piscataway, NJ* **2002**, pp. II-II.
- [119] B. Ruhstaller, T. Beierlein, H. Riel, S. Karg, J. C. Scott, W. Riess, *IEEE J. Sel. Top. Quantum Electron.* **2003**, 9, 723.
- [120] O. Almora, D. Miravet, I. Gelmetti, G. Garcia-Belmonte, *Phys. Status Solidi RRL* **2022**, 16, 2200336.
- [121] D. Moia, I. Gelmetti, P. Calado, Y. Hu, X. Li, P. Docampo, J. de Mello, J. Maier, J. Nelson, P. R. F. Barnes, *Phys. Rev. Appl.* **2022**, 18, 044056.
- [122] S. van Reenen, M. Kemerink, H. J. Snaith, *J. Phys. Chem. Lett.* **2015**, 6, 3808.
- [123] G. Richardson, S. E. J. O'Kane, R. G. Niemann, T. A. Peltola, J. M. Foster, P. J. Cameron, A. B. Walker, *Energy Environ. Sci.* **2016**, 9, 1476.
- [124] D. A. Jacobs, Y. Wu, H. Shen, C. Barugkin, F. J. Beck, T. P. White, K. Weber, K. R. Catchpole, *Phys. Chem. Chem. Phys.* **2017**, 19, 3094.
- [125] N. E. Courtier, G. Richardson, J. M. Foster, *Appl. Math. Modell.* **2018**, 63, 329.
- [126] S. Almosni, L. Cojocar, D. Li, S. Uchida, T. Kubo, H. Segawa, *Energy Technol.* **2017**, 5, 1767.
- [127] N. E. Courtier, J. M. Cave, J. M. Foster, A. B. Walker, G. Richardson, *Energy Environ. Sci.* **2019**, 12, 396.
- [128] N. E. Courtier, J. M. Cave, A. B. Walker, G. Richardson, J. M. Foster, *J. Comput. Electron.* **2019**, 18, 1435.
- [129] D. Moia, I. Gelmetti, P. Calado, W. Fisher, M. Stringer, O. Game, Y. Hu, P. Docampo, D. Lidzey, E. Palomares, J. Nelson, P. R. F. Barnes, *Energy Environ. Sci.* **2019**, 12, 1296.
- [130] P. Calado, I. Gelmetti, B. Hilton, M. Azzouzi, J. Nelson, P. R. F. Barnes, *J. Comput. Electron.* **2022**, 21, 960.
- [131] W. Clarke, L. J. Bennett, Y. Grudeva, J. M. Foster, G. Richardson, N. E. Courtier, *J. Comput. Electron.* **2023**, 22, 364.
- [132] J. Baik, H. Jun, H. Nahdi, B. Geffroy, D. Tondelier, Y. Bonnassieux in *Journées Nationales du Photovoltaïque*, HAL open science, Dourdan, France **2021**, cea-03123520f. <https://hal-cea.archives-ouvertes.fr/cea-03123520>
- [133] S. Altazin, C. Kirsch, E. Knapp, A. Stous, B. Ruhstaller, *J. Appl. Phys.* **2018**, 124, 135501.
- [134] C. Vael, S. Jenatsch, S. Züfle, F. Nüesch, B. Ruhstaller, *J. Appl. Phys.* **2022**, 131, 205702.
- [135] M. S. Salem, A. Shaker, M. Abouelatta, A. Saeed, *Polymers* **2023**, 15, 784.
- [136] M. T. Neukom, A. Schiller, S. Züfle, E. Knapp, J. Ávila, D. Pérez-del-Rey, C. Dreessen, K. P. Zanon, M. Sessolo, H. J. Bolink, *ACS Appl. Mater. Interfaces* **2019**, 11, 23320.
- [137] A. Riquelme Expósito, L. Bennett, N. Courtier, M. Wolf, L. Contreras Bernal, A. Walker, G. Richardson, J. Anta, *arXiv:2003.07386*, **2020**.
- [138] K. Miyano, M. Yanagida, Y. Shirai, *Adv. Energy Mater.* **2020**, 10, 1903097.
- [139] A. J. Riquelme, K. Valadez-Villalobos, P. P. Boix, G. Oskam, I. Mora-Seró, J. A. Anta, *Phys. Chem. Chem. Phys.* **2022**, 24, 15657.
- [140] J. Diekmann, F. Peña-Camargo, N. Tokmoldin, J. Thiesbrummel, J. Warby, E. Gutierrez-Partida, S. Shah, D. Neher, M. Stollerfoht, *J. Phys. Chem. Lett.* **2023**, 14, 4200.
- [141] S. Ravishankar, A. Riquelme, S. K. Sarkar, M. Garcia-Battle, G. Garcia-Belmonte, J. Bisquert, *J. Phys. Chem. C* **2019**, 123, 24995.
- [142] N. Parikh, S. Narayanan, H. Kumari, D. Prochowicz, A. Kalam, S. Satapathi, S. Akin, M. M. Tavakoli, P. Yadav, *Phys. Status Solidi RRL* **2022**, 16, 2100510.
- [143] A. Bou, A. Pockett, D. Raptis, T. Watson, M. J. Carnie, J. Bisquert, *J. Phys. Chem. Lett.* **2020**, 11, 8654.
- [144] A. Albadri, P. Yadav, M. Alotaibi, N. Arora, A. Alyamani, H. Albrithen, M. I. Dar, S. M. Zakeeruddin, M. Grätzel, *J. Phys. Chem. C* **2017**, 121, 24903.
- [145] E. Guillén, F. J. Ramos, J. A. Anta, S. Ahmad, *J. Phys. Chem. C* **2014**, 118, 22913.
- [146] S. Ravishankar, C. Aranda, P. P. Boix, J. A. Anta, J. Bisquert, G. Garcia-Belmonte, *J. Phys. Chem. Lett.* **2018**, 9, 3099.
- [147] J. Zhang, M.-h. Shang, P. Wang, X. Huang, J. Xu, Z. Hu, Y. Zhu, L. Han, *ACS Energy Lett.* **2016**, 1, 535.
- [148] B.-E. Cohen, Y. Li, Q. Meng, L. Etgar, *Nano Lett.* **2019**, 19, 2588.
- [149] M. Kim, G.-H. Kim, K. S. Oh, Y. Jo, H. Yoon, K.-H. Kim, H. Lee, J. Y. Kim, D. S. Kim, *ACS Nano* **2017**, 11, 6057.
- [150] Z. Ye, J. Zhou, J. Hou, F. Deng, Y.-Z. Zheng, X. Tao, *Sol. RRL* **2019**, 3, 1900109.

- [151] U. K. Thakur, P. Kumar, S. Gusarov, A. E. Kobryn, S. Riddell, A. Goswami, K. M. Alam, S. Savela, P. Kar, T. Thundat, A. Meldrum, K. Shankar, *ACS Appl. Mater. Interfaces* **2020**, *12*, 11467.
- [152] D. Prochowicz, M. M. Tavakoli, M. Wolska-Pietkiewicz, M. Jędrzejewska, S. Trivedi, M. Kumar, S. M. Zakeeruddin, J. Lewiński, M. Graetzel, P. Yadav, *Sol. Energy* **2020**, *197*, 50.
- [153] Y. Jo, K. S. Oh, M. Kim, K.-H. Kim, H. Lee, C.-W. Lee, D. S. Kim, *Adv. Mater. Interfaces* **2016**, *3*, 1500768.
- [154] J. Huang, H. Yan, D. Zhou, J. Zhang, S. Deng, P. Xu, R. Chen, H.-S. Kwok, G. Li, *ACS Appl. Mater. Interfaces* **2020**, *12*, 40364.
- [155] G.-O. Kim, K.-S. Ryu, *Bull. Korean Chem. Soc.* **2012**, *33*, 469.
- [156] A. Pockett, G. E. Eperon, T. Peltola, H. J. Snaith, A. Walker, L. M. Peter, P. J. Cameron, *J. Phys. Chem. C* **2015**, *119*, 3456.
- [157] J. Krüger, R. Plass, M. Grätzel, P. J. Cameron, L. M. Peter, *J. Phys. Chem. B* **2003**, *107*, 7536.
- [158] Y. T. Set, B. Li, F. J. Lim, E. Birgersson, J. Luther, *Appl. Phys. Lett.* **2015**, *107*, 173301.
- [159] X. Chen, Y. Shirai, M. Yanagida, K. Miyano, *Phys. Chem. Chem. Phys.* **2018**, *20*, 17918.
- [160] E. Kamieniecki, *J. Vac. Sci. Technol.* **1982**, *20*, 811.
- [161] E. Kamieniecki, *J. Appl. Phys.* **1983**, *54*, 6481.
- [162] R. Peat, L. Peter, *J. Electroanal. Chem. Interfacial Electrochem.* **1987**, *228*, 351.
- [163] E. Ponomarev, L. Peter, *J. Electroanal. Chem.* **1995**, *396*, 219.
- [164] L. Dloczik, O. Ieperuma, I. Lauer mann, L. Peter, E. Ponomarev, G. Redmond, N. Shaw, I. Uhlendorf, *J. Phys. Chem. B* **1997**, *101*, 10281.
- [165] P. De Jongh, D. Vanmaekelbergh, *J. Phys. Chem. B* **1997**, *101*, 2716.
- [166] Y. Gao, A. J. Wise, A. K. Thomas, J. K. Grey, *ACS Appl. Mater. Interfaces* **2016**, *8*, 285.
- [167] L. Bertoluzzi, J. Bisquert, *J. Phys. Chem. Lett.* **2017**, *8*, 172.
- [168] S. Ravishankar, C. Aranda, S. Sanchez, J. Bisquert, M. Saliba, G. Garcia-Belmonte, *J. Phys. Chem. C* **2019**, *123*, 6444.
- [169] H. Song, D. D. Macdonald, *J. Electrochem. Soc.* **1991**, *138*, 1408.
- [170] J. Halme, *Phys. Chem. Chem. Phys.* **2011**, *13*, 12435.
- [171] J. Halme, K. Miettunen, P. Lund, *J. Phys. Chem. C* **2008**, *112*, 20491.
- [172] C. Donolato, *Appl. Phys. Lett.* **1985**, *46*, 270.
- [173] A. O. Alvarez, S. Ravishankar, F. Fabregat-Santiago, *Small Methods* **2021**, *5*, 2100661.
- [174] A. Bou, H. Āboliņš, A. Ashoka, H. Cruanyes, A. Guerrero, F. Deschler, J. Bisquert, *ACS Energy Lett.* **2021**, *6*, 2248.
- [175] S. M. Abdulrahim, Z. Ahmad, J. Bahadra, N. J. Al-Thani, *Nanomaterials* **2020**, *10*, 1635.
- [176] C.-I. So, P. Kim, K.-I. Ryu, K.-S. Sonu, J.-H. Ri, S.-H. Kim, Y.-H. Jong, *J. Electron. Mater.* **2022**, *51*, 6020.
- [177] M. A. Afroz, C. A. Aranda, N. K. Tailor, Yukta, P. Y., M. M. Tavakoli, M. Saliba, S. Satapathi, *ACS Energy Lett.* **2021**, *6*, 3275.
- [178] S. Yuan, J. Wang, K. Yang, P. Wang, X. Zhang, Y. Zhan, L. Zheng, *Nanoscale* **2018**, *10*, 18909.
- [179] C. Aranda, A. Guerrero, J. Bisquert, *ACS Energy Lett.* **2019**, *4*, 741.
- [180] L. Liang, H. Luo, J. Hu, H. Li, P. Gao, *Adv. Energy Mater.* **2020**, *10*, 2000197.
- [181] G. Liu, H. Zheng, H. Xu, L. Zhang, X. Xu, S. Xu, X. Pan, *Nano Energy* **2020**, *73*, 104753.
- [182] S. Zouhair, S. M. Yoo, D. Bogachuk, J. P. Herterich, J. Lim, H. Kanda, B. Son, H. J. Yun, U. Würfel, A. Chahboun, *Adv. Energy Mater.* **2022**, *12*, 2200837.
- [183] S. Xiong, Y. Dai, J. Yang, W. Xiao, D. Li, X. Liu, L. Ding, P. Gao, M. Fahlman, Q. Bao, *Nano Energy* **2021**, *79*, 105505.
- [184] A. O. Alvarez, R. Arcas, C. A. Aranda, L. Bethencourt, E. Mas-Marzá, M. Saliba, F. Fabregat-Santiago, *J. Phys. Chem. Lett.* **2020**, *11*, 8417.
- [185] O. Almora, *OAJ Mater. Devices* **2021**, *5*, 723.
- [186] L. Contreras-Bernal, M. Salado, A. Todinova, L. Calio, S. Ahmad, J. Idígoras, J. A. Anta, *J. Phys. Chem. C* **2017**, *121*, 9705.
- [187] Y. Li, Y. Li, J. Shi, H. Li, H. Zhang, J. Wu, D. Li, Y. Luo, H. Wu, Q. Meng, *Appl. Phys. Lett.* **2018**, *112*, 053904.
- [188] D. Pitarch-Tena, T. T. Ngo, M. Vallés-Pelarda, T. Pauporté, I. Mora-Sero, *ACS Energy Lett.* **2018**, *3*, 1044.
- [189] J. Bisquert, *Phys. Chem. Chem. Phys.* **2003**, *5*, 5360.



**Elnaz Ghahremani Rad** is a Ph.D. candidate in the group of Dr. Alexander R. Uhl at the University of British Columbia in the Laboratory of Solar Energy and Fuels (LSEF). Her main research interests are numerical modeling, characterization, and fabrication of optoelectronic devices with a focus on solar cells. She is currently working on impedance spectroscopy characterization and modeling of perovskite solar cells to study degradation processes and improve device stability.





**Osbel Almora** graduated in physics from the University of Havana, Cuba (2013), obtained a master's degree in applied physics from the Universitat Jaume I of Castelló, Spain (2016), and received his Dr.-Ing. degree from the Friedrich-Alexander Universität Erlangen-Nürnberg, Germany (2020). He is currently a Juan de la Cierva postdoctoral fellow at the Universitat Rovira i Virgili of Tarragona, Spain. His main research interests are the optoelectronic characterization and modeling of semiconductor materials and devices, with a special focus on photovoltaics. He is a starting member of the emerging-pv.org initiative.



**Sunil Suresh** is a Ph.D. student at the University of British Columbia (UBC), at the Laboratory for Solar Energy and Fuels (LSEF). He received his M.Sc. from TU Delft in 2018 and was a member of the Alternative Thin-Film Photovoltaics group at IMEC, Belgium (2018–2019). His research interests include solution-processed thin-film photovoltaics and the implementation of advanced architectures (surface passivation) for chalcogenide solar cells.



**Amandine A. Drew** is a MASc student at the University of British Columbia (UBC) in the Laboratory for Solar Energy and Fuels (LSEF). She completed her Bachelor of Engineering Science in mechanical engineering at Western University in 2020. Her research focuses on PV system design and optimization.



**Towhid H. Chowdhury** is a postdoctoral researcher who works at the Laboratory of Solar Energy and Fuels (LSEF), at the University of British Columbia (UBC) Okanagan, Canada. Before joining UBC, he used to work with the National Institute for Materials Science (NIMS), Japan (2018–2021), Kyoto University, Japan (2021), and Pohang University of Science and Technology (POSTECH), South Korea (2022) as a researcher. He has a keen research interest in perovskite semiconductors for optoelectronics and electric applications.



**Alexander R. Uhl** is an assistant professor, Principal's Research Chair in Solar Energy Conversion (Tier 2), and head of the Laboratory for Solar Energy and Fuels (LSEF) at the University of British Columbia (UBC) Okanagan, Canada. He obtained his Ph.D. in 2013 from ETH Zurich and was a postdoctoral fellow with Prof. Hugh Hillhouse at the University of Washington and Prof. Michael Graetzel at the École Polytechnique Fédérale de Lausanne (EPFL). His group's research focuses on solution-processed thin film layers for application in photovoltaic devices and solar fuels. <https://lsef.ok.ubc.ca/>